J. Fluid Mech. (1989), *vol.* 208, *pp.* 321–354
Printed in Great Britain

The fluid mechanics of slide coating

By K. N. CHRISTODOULOU† AND L. E. SCRIVEN
Center for Interfacial Engineering, Minnesota Supercomputer Institute *and* Department of Chemical Engineering & Materials Science, University of Minnesota, Minneapolis, MN 55455, USA

(Received 18 November 1988)

Slide coating is a means of rapidly depositing multilayered liquid films of precise thickness and uniformity, as in manufacture of photographic products. Liquid is metered through one or more slots onto the inclined surface of the coating die, flows down that face and across a gap onto a fast-moving smooth surface. In this paper the steady, two-dimensional slide coating flow of a Newtonian liquid is analysed by solving the full Navier–Stokes system with the Galerkin/finite-element technique, spine parametrization of free surfaces and full Newton iteration. The lower meniscus in the gap is assumed to remain pinned at the die edge and the wetting-line singularity on the surface being coated is relieved by introducing dynamic-slip and contact-angle parameters. Results include the effects of several design and operating parameters on free-surface profiles and details of the flow field; these are presented by means of contours of kinematic and dynamic variables and local force balances over subdomains. The profiles show standing waves on the slide, rapid film thinning just before the gap, and exponential approach to the final film thickness on the web. As Reynolds number is raised and/or web speed is lowered several recirculation regions are predicted, deleterious features that have also been detected in experiments.

1. Introduction

Coating is any process that replaces gas at a solid surface by a layer of liquid. Usually the layer is required to be thin, continuous, uniform in thickness or smooth at its free surface, and to remain that way until it can be solidified into a more or less permanent coating. Slide coating is the process in which liquid issues at premetered rate through one or more slots of an applicator die onto the inclined face of the die, flows laminarly as a film down that face and across a narrow gap onto a smooth-surfaced substrate that is translating rapidly at constant speed in its own plane: see figure 1. The substrate, a flexible 'web', moves on into a chilling, drying, or curing zone where the liquid on it is solidified. Slide coating is widely used in the continuous, high-speed manufacture of photographic, graphic arts, and X-ray films as well as other precision products.

Colour photographic films and certain other products are based on multiple layers, each with a different function to perform. Provided the layers can be formed of miscible liquids, i.e. without interfacial tension between them, it may be possible to avoid multiple-pass deposition and solidification of successive layers and instead coat them simultaneously. If this is possible, the leading means is a multilayer or cascade coating die of the sort diagrammed in figure 1. The top surface is an inclined plane, called the slide, which is interrupted by narrow slots through which are carefully

† Present address: E.I. du Pont de Nemours & Co. Inc., Wilmington, DE 19898, USA.

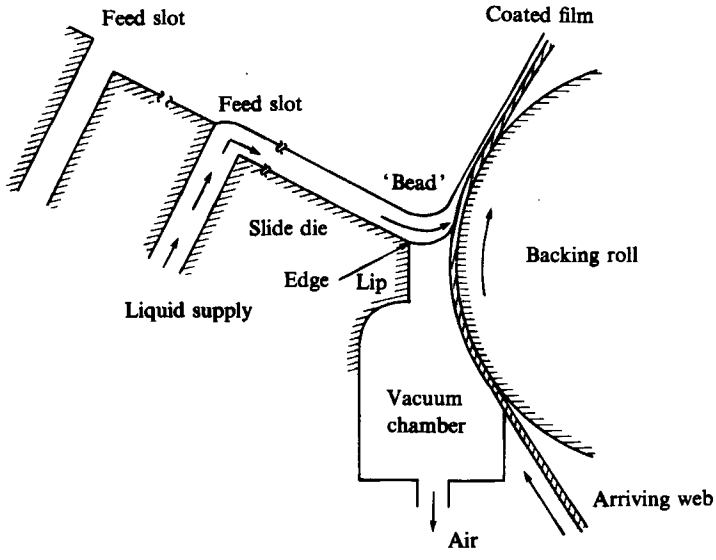

FIGURE 1. Multilayer slide coater system.

pumped the liquid compositions of successive layers. Each turns and flows laminarly downward in a thin layer that successively encounters others formed in the same way. When the slots are properly designed, the oncoming liquid rides up onto each issuing layer without mixing (though with interdiffusion, a minor effect) so that a multilayer film is formed. This flows to the lower end, or lip edge, of the die and on into the 'coating bead' or 'coating meniscus' that bridges the narrow gap between the lip and the web being coated. The latter wraps a roller that is precisely positioned to maintain the gap.

On the web side of the gap the liquid contacts, wets and coats the fast-moving substrate uniformly across its entire width, excepting unavoidable edge zones, or so it should in successful coating operations, and then the flow is steady and two-dimensional. A small vacuum is usually applied beneath the liquid bridge or coating bead in order to keep it stable at higher coating speed and perhaps higher viscosity and lower surface tension and wider gap than would otherwise be possible. This tactic was disclosed by Beguin (1954) in a landmark patent. Many variations of the basic configuration and lip shape have since been described (e.g. Russell, Wilson & Carleton 1956; Mercier, Torpey & Russell 1956; Jackson, Winkler & Woodworth 1976; Choinski 1979; Isayama & Takehara 1981; Burket, Conaghan & Hirshburg 1984; Hitaka & Namiki 1984).

Three flow regions can be distinguished in the liquid flow of the slide coating process. The feed, or slide, region establishes a velocity distribution and a thickness distribution that are uniform in the transverse direction except for edge effects. The meniscus, or bead, region ensures the equality of the average rate at which liquid arrives at the lip and the average rate at which it is picked up and carried away by the moving web. The film development, or web, region encompasses the approach of the film to fully developed flow, which would be plug flow at the substrate speed except for a small effect of gravity.

Though this process is routinely used in the manufacture of photographic products, its steady flow and instabilities are still matters of controversy (aired at the First Symposium on Fundamentals of Coating in Orlando, Florida in 1982). Strong nonlinearities contributed by the free surfaces even when inertia is small, and

apparent stress singularities at static separation lines and dynamic wetting lines make a fluid mechanical theory of slide coating flow a real challenge. Only recently have means been developed for efficiently making reliably accurate theoretical predictions of such complicated flows – excepting, perhaps, the neighbourhoods of dynamic apparent contact lines or wetting lines, where empirical parameters have to be employed as expedients (Kistler & Scriven 1983).

Previous studies of slide coating systems are few. Faust (1975) working with J. A. Tallmadge investigated experimentally the shapes of the free surfaces and the influences of some operating variables on bead operability limits. Though she measured speed limits of several Newtonian liquids with different viscosities over a range of flow rates and gap widths, she applied no vacuum under the coating bead.

In a precursor of the present paper Kobayashi, Saito & Scriven (1982) analysed a restricted set of slide coating flows by using the method of subdomains, free-surface parametrization by spines, local polynomial basis functions, isoparametric mapping, and Galerkin's method of weighted residuals with Gaussian quadrature – altogether the Galerkin/finite-element technique. On the assumption that the lower meniscus of the coating bead pins to a sharpened lip, or edge of the coating die, they computed predictions of effects of changing a limited number of parameters on free-surface shapes and velocity fields.

Galehouse & Colt (1984) worked out film-flow approximations for flow in the slide region and web region: they neglected inertial effects, balanced viscous force and capillary pressure gradient, and linearized the equations around the asymptotic regimes. For the vicinity of the dynamic wetting line they used a variant of Moffat's (1964) corner flow model, as had Huh & Scriven (1971) originally. Galehouse & Colt found that their approximations matched measured profiles downstream in the web region but not upstream in the slide region.

More recently, Bach & Hassager (1985) used a so-called Langrangian finite-element scheme, based on a succession of material coordinates, to attack several flows including a slide coating prototype. The scheme employs initial-value problems to arrive at steady states and so is unsatisfactory for surveying those parts of a state space populated by unstable or nearly unstable steady states. For the vicinity of the dynamic wetting line Bach & Hassager used slip and excessively refined subdomaining, or gridding, in an attempt to match Moffat's (1964) corner flow model. Comparable matching can be achieved through 'singular' elements, as we shall describe in a future publication.

Hens & Boiy (1986) observed how the curvature of the upper meniscus of the bead region depends on several operating variables; they also put forward a simplified analysis of the growth of the boundary layer in the bead region downstream of the dynamic wetting line, an analysis paralleling Kistler's (1984) of the same phenomenon in curtain coating flow.

Schweitzer (1988) developed a technique for visualizing small-scale film flows. By using hydrogen bubbles, dye injection and optical sectioning, he was able to display the interior of the two-dimensional flow field of a slide coater via streamlines; his photographs also displayed the shape of free surfaces including dynamic and static wetting lines and apparent contact angles.

In the present paper we report a computer-aided theoretical analysis of steady, two-dimensional flow of Newtonian coating liquid through the three regions of a slide coater. The prototype system is diagrammed in figure 2. It consists of a single liquid layer of uniform viscosity, density, and surface tension being coated onto the surface of a perfectly flat web (extension to multiple layers is straightforward with

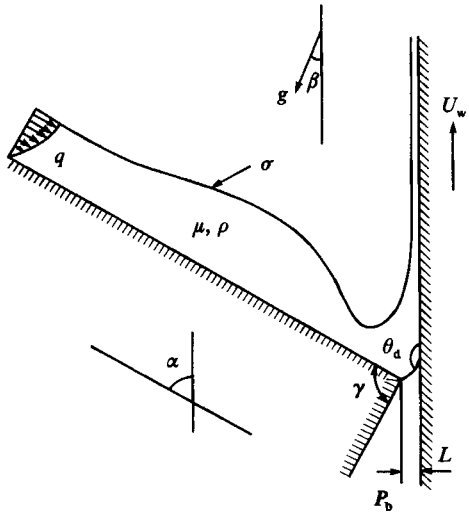

FIGURE 2. Prototype slide coater and flow parameters.

streamline elements (Kistler & Scriven 1983; Papanastasiou 1984). Steady states of this system are described by solutions of a non-standard elliptic boundary-value problem: parts of the boundary are free and parts are synthetic boundaries with upstream and downstream regions that are most efficiently treated as obeying approximate equations. We solved the compound problem by a Galerkin/finite-element method, which leads to a large set of algebraic equations, many of them nonlinear. We used Newton iteration with continuation to solve all the equations simultaneously for the shapes of the free surfaces, the velocity field and the pressure field. Newton iteration offers not only rapid – though local – convergence but also potent byproducts. Its Jacobian matrix can be used to detect loss of the two-dimensional, steady solution as parameters are varied, and appearance of multiple two-dimensional steady-state solutions (i.e. turning points and certain kinds of bifurcations). It has other uses as well (Brown, Scriven & Silliman 1980).

Section 2 compiles the governing equations. Section 3 summarizes the derivation, linearization, and analytical solution of one-dimensional, asymptotic film profile equations for upstream flow on the slide and downstream flow on the web. The results are predictions of standing waves on the slide and an exponential approach to the final film thickness on the web; they provide natural boundary conditions for the Galerkin/finite-element formulation of the two-dimensional flow in the bead region and nearby. Section 4 describes that formulation and its solution. Section 5 presents results: free-surface profiles, contours of kinematic and dynamic variables and local force balances over subdomains, all organized to illuminate how the leading design and operating parameters affect the flow.

2. Prototype slide coater

Even when most of the flow is virtually two-dimensional, edge effects make it three-dimensional because slide coaters are finite in width. Irregularities of the web surface cause three-dimensional and time-dependent flow. High deformation rates near the wetting line may give rise to non-Newtonian stress there even when otherwise the liquid seems Newtonian. Variations in surface composition, par-

ticularly where free surfaces are being rapidly extended as near the wetting line, may cause surface-tension gradients. All these complications and yet others we leave to sequels and here narrow attention to the system of figure 2.

The relevant Navier–Stokes system is, in dimensionless form,

$$Re\,\boldsymbol{u}\cdot\boldsymbol{\nabla u} = \boldsymbol{\nabla}\cdot\boldsymbol{T} + 3/\cos(\alpha+\beta)\boldsymbol{f}, \tag{1}$$

$$\boldsymbol{\nabla}\cdot\boldsymbol{u} = 0, \tag{2}$$

with traction, impenetrability and no-slip boundary conditions:

$$\boldsymbol{n}\cdot\boldsymbol{\nabla T} = \frac{1}{Ca}\frac{\mathrm{d}\boldsymbol{t}}{\mathrm{d}s} + p_{\mathrm{a}}\boldsymbol{n}, \quad \text{at free surfaces,} \tag{3}$$

$$\boldsymbol{n}\cdot\boldsymbol{u} = 0, \quad \text{at free surfaces,} \tag{4}$$

$$\boldsymbol{u} = \boldsymbol{u}_{\mathrm{s}} \quad \text{at solid surfaces} \tag{5}$$

(the region near the dynamic apparent contact line is an exception to (5): see below). $\boldsymbol{u}$ is the velocity measured in units of $U \equiv q/h_0 = [\rho g q^2 \cos(\alpha+\beta)/3\mu]^{\frac{1}{3}}$, the average velocity of the fully developed film on the slide; length as in $\boldsymbol{\nabla}$ is measured in units of the thickness $h_0 \equiv [3\mu q/\rho g \cos(\alpha+\beta)]^{\frac{1}{3}}$ of that film, q being the volumetric flow rate per unit width, β the gravity-web angle, α the web-slide angle, and g the gravitational acceleration; $\boldsymbol{f} \equiv -\sin\beta\boldsymbol{i} - \cos\beta\boldsymbol{j}$ is the unit vector in the direction of gravity; $\boldsymbol{i}$ and $\boldsymbol{j}$ are the unit vectors in the directions normal and parallel to the web. The liquid properties are density ρ, viscosity μ, and surface tension σ. The stress tensor is $\boldsymbol{T} = -p\boldsymbol{I} + [\boldsymbol{\nabla u} + (\boldsymbol{\nabla u})^{\mathrm{T}}]$, where p is the pressure and $\boldsymbol{I}$ the unit tensor. Both stress and pressure are measured in units of $\mu q/h_0^2$. $Re \equiv \rho q/\mu$ is the Reynolds number, $Ca \equiv \mu U/\sigma$ the capillary number, p_{a} the ambient pressure, and $\boldsymbol{u}_{\mathrm{s}}$ the velocity of solid boundaries. $\boldsymbol{n}$ is the local unit normal to the boundary, $\boldsymbol{t}$ the local unit tangent, and s the arclength along the boundary. The curvature of the boundary is then $\mathrm{d}\boldsymbol{t}/\mathrm{d}s$.

Conventional fluid mechanical theory would allow no slip between liquid and solid (equation (5)), but were this strictly true at the dynamic wetting line the drag force on the substrate would be unbounded and coating would be impossible (Huh & Scriven 1971). Such singularities usually signal failure of one or more hypotheses of the model. No slip is the main suspect here and air entrainment its likely accomplice; but there are other suspects too: non-Newtonian behaviour of the liquid due to high rates of strain or long-range intermolecular forces (electrostatic and dispersion) that in the guise of disjoining phenomena take on special importance in the thin films that underlie an apparent contact line; cavitation due to very low pressures and high viscous dissipation. In this paper we employ near the wetting line Navier's (1827) boundary condition that makes the flux of momentum tangential to the wall proportional to the velocity discontinuity, as formulated earlier (Silliman & Scriven 1980):

$$(1/\beta_{\mathrm{slip}})\,\boldsymbol{t}_{\mathrm{s}}\cdot(\boldsymbol{u}-\boldsymbol{u}_{\mathrm{s}}) = \boldsymbol{t}_{\mathrm{s}}\boldsymbol{n}_{\mathrm{s}}:\boldsymbol{T}. \tag{6}$$

β_{slip} is the slip coefficient and $\boldsymbol{t}_{\mathrm{s}}$ and $\boldsymbol{n}_{\mathrm{s}}$ are the unit tangent and unit normal to the solid surface. For the present purpose β_{slip} is an empirical parameter, sensitivity to which must be tested. Equation (6) makes the singularity integrable but implies zero velocity at the contact line. This result is inconsistent with macroscopic observations (Burley & Kennedy 1976) that reveal no deceleration of the liquid approaching the wetting line. Recent laser-Doppler velocimetry measurements (Hens & Mues 1988), however, support the idea of a velocity discontinuity and the hypothesis that it is caused by an invisibly thin film of entrained air that rapidly breaks down (Miyamoto

& Scriven 1982; Miyamoto 1986). An alternative is to assume no slip at the macroscopic scale; this gives rise to a discontinuous velocity field at the wetting line, but such a device can be handled with special techniques developed in the fracture mechanics literature for handling singularities (e.g. Bathe 1982, p. 226).

The angle of contact between the liquid/air interface and the solid surface is also needed as a boundary condition on the interfacial shape at the wetting line:

$$\boldsymbol{n}_{\mathrm{d}} \cdot \boldsymbol{n}_{\mathrm{w}} = \cos\theta_{\mathrm{d}}. \tag{7}$$

Here, $\boldsymbol{n}_{\mathrm{d}}$ and $\boldsymbol{n}_{\mathrm{w}}$ are the outward unit normals at the wetting line to the visible free surface and the solid surface respectively. However, the apparent contact angle θ_{d} is seen to vary with the flow field and surface properties in a still poorly understood way (Burley & Kennedy 1976; Gutoff & Kendrick 1982). Here it is employed as an empirical parameter, sensitivity to which must be tested.

Far upstream on the slide the flow relaxes to almost fully developed film flow:

$$h = 1, \quad u = 3(y - \tfrac{1}{2}y^2), \quad v = 0. \tag{8}$$

In practice, (8) are imposed at a finite distance (ordinarily $10h_0$–$15h_0$) upstream from the die lip at a location called the inflow boundary. Similarly, far downstream on the web the flow satisfies the following asymptotic conditions of zero traction and free-surface slope in the streamwise direction:

$$\boldsymbol{n} \cdot \boldsymbol{T} = \boldsymbol{0} \text{ or } \boldsymbol{nn} : \boldsymbol{T} = 0, \quad \boldsymbol{t}_1 \times \boldsymbol{v} = \boldsymbol{0}; \; \boldsymbol{t} = \boldsymbol{t}_1. \tag{9}$$

Here $\boldsymbol{t}$ is the unit vector tangent to the free surface at the outflow plane, $\boldsymbol{t}_1$ is the unit vector parallel to the web, and $\boldsymbol{n}$ the unit vector normal to the outflow plane. Equations (9) are imposed as natural boundary conditions (second kind or Neumann conditions) because these prove preferable to essential ones (first kind or Dirichlet conditions) that specify the asymptotic velocity and free-surface position. This is also done at a finite distance downstream of the wetting line at a location called the outflow boundary. Both inflow and outflow boundaries are artificial and sensitivity of solutions to their locations must be tested.

The lip of the prototype coating die is taken to be unwettable by the coating liquid and so the lower meniscus is pinned at the edge, i.e. the static contact line locates there. This essential condition on the free-surface location overrides the kinematic equation there and no static contact angle is needed. The equally important case of a freely locatable static contact line that makes a prescribed static contact angle is treated in a sequel (Christodoulou & Scriven 1989*a*).

3. Asymptotic solutions for slide and web regions

Far upstream on the slide and far downstream on the web the flow relaxes to almost fully developed film flow. The governing equations can be simplified and even solved analytically there (Ruschak 1978; Higgins & Scriven 1979; Kheshgi & Scriven 1979). Those analytical solutions can in turn serve as natural boundary conditions at the inflow and outflow boundaries. In this way the computational domain can be shortened and the cost of the finite-element analysis reduced without loss in accuracy.

3.1. *Flow on the slide*

The Navier–Stokes equations and boundary conditions with the scaling in §2 take the form (Ruschak 1978):

$$\left.\begin{aligned}
&Re\,(uu_x+vu_y) = -p_x+u_{yy}+u_{xx}+3,\\
&Re\,(uv_x+vv_y) = -p_y+v_{yy}+v_{xx}+3\tan(\alpha+\beta), \quad u_x+v_y = 0,\\
&p+2u_x(1+h_x^2)/(1-h_x^2)+\kappa/Ca = 0, \quad \kappa = h_{xx}(1+h_x^2)^{-\frac{3}{2}},\\
&(u_y+v_x)(1-h_x^2)-4h_x u_x = 0, \quad v = h_x u,\\
&u\to 3(y-\tfrac{1}{2}y^2), \quad v\to 0, \quad h\to 1 \quad (x\to-\infty),\\
&u = 0, \quad v = 0 \quad (y = 0).
\end{aligned}\right\} \tag{10}$$

Here x and y are parallel and normal to the slide surface. For small slope $u\sim 1$ and $v\sim h_x u$. On the assumption that each y-differentiation of an independent variable is of order unity, whereas each x-differentiation is of order $|h_x|\ll 1$, system (10) becomes

$$Re\,(uu_x+vu_y) = -p_x+u_{yy}+3, \tag{11a}$$

$$0 = -p_y-3\tan(\alpha+\beta), \quad u_x+v_y = 0, \tag{11b, c}$$

$$p+\kappa/Ca = 0, \quad u_y = 0, \quad v = h_x u \quad (y = h), \tag{11d, e, f}$$

$$u\to 3(y-\tfrac{1}{2}y^2), \quad v\to 0, \quad h\to 1 \quad (x\to-\infty), \tag{11g, h, i}$$

$$u = 0, \quad v = 0 \quad (y = 0). \tag{11j, k}$$

From (11*b*, *d*) it follows that

$$p_x = -\kappa_x/Ca+3\tan(\alpha+\beta)\,h_x. \tag{12}$$

Substituting p_x from (12) into (11*a*), introducing the following approximate velocity profile, which satisfies (11*e–i*):

$$u = 3/h[y/h-\tfrac{1}{2}(y/h)^2], \tag{13a}$$

$$v = y/hh_x u; \tag{13b}$$

and integrating across the liquid film results in an ordinary differential equation for the film profile (cf. Higgins & Scriven 1979):

$$h_{xxx} = 3Ca\left[-1 + \frac{1}{h^3} - \frac{2}{5}Re\frac{h_x}{h^3} + h_x\tan(\alpha+\beta)\right]. \tag{14}$$

capillary pressure gradient	streamwise gravity force	viscous shear at wall	streamwise momentum convection	cross-stream gravity force

Linearizing (14) for small deviations $\epsilon\equiv h-1\ll h_0$ from the fully developed film flow far upstream on the slide yields

$$\epsilon_{xxx}+3Ca[\tfrac{2}{5}Re-\tan(\alpha+\beta)]\,\epsilon_x+9Ca\epsilon = 0 \tag{15}$$

along with the boundary conditions

$$\epsilon = 0, \quad \epsilon_x = 0 \quad \text{as} \quad x\to-\infty \quad \text{(far upstream)}. \tag{16}$$

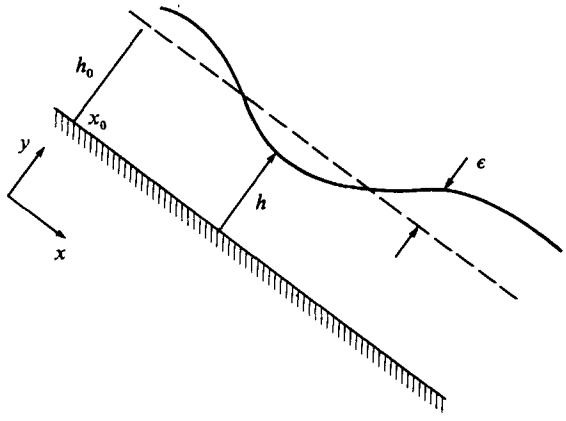

FIGURE 3. Solution of asymptotic equation far upstream on the slide, $\epsilon = \epsilon_0 \exp(\gamma x)\cos(\delta x + \phi)$.

The solution of (14) that satisfies (15) is

$$\epsilon = \epsilon_0 \exp(-\gamma x)\cos(\delta x + \phi). \tag{17}$$

The constants γ and δ come from the flow parameters Ca and Re:

$$\gamma = \tfrac{1}{2}(A+B), \quad \delta = \tfrac{1}{2}\sqrt{3}(A-B), \tag{18}$$

where

$$A,B \equiv \{-\tfrac{9}{2}Ca \pm [(\tfrac{9}{2}Ca)^2 + [\tfrac{2}{5}Ca\,Re - Ca\tan(\alpha+\beta)]^3]^{\frac{1}{2}}\}^{\frac{1}{3}}, \tag{19}$$

and ϵ_0 and ϕ are determined from the thickness and slope of the film at the place chosen to be $x = x_0$ (see figure 3). Taking this point on the inflow boundary of the two-dimensional flow domain (§4) is the key to matching the analytical and numerical solutions.

According to (17) there is a train of standing waves decaying in the upstream direction when the square-root in (19) is real. It is instructive to examine the form of this solution at various limits of the parameters and to compare it with other solutions in the literature. When inertial and cross-stream gravitational terms in (14) are neglected, (17) becomes

$$\epsilon = \epsilon_0 \exp[\tfrac{1}{2}(9Ca)^{\frac{1}{3}}x]\cos[\tfrac{1}{2}\sqrt{3}\,\tfrac{1}{2}(9Ca)^{\frac{1}{3}}x + \phi], \tag{20}$$

which is Galehouse & Colt's (1984) result.

As Re rises the decay rate γ becomes small and the train of standing waves persists for long distances upstream. The wavelength can be estimated from

$$\lambda = \frac{2\pi}{\delta} \approx \frac{2\pi}{(\frac{6}{5}Ca\,Re)^{\frac{1}{2}}} \quad \text{when} \quad Re \gg 1. \tag{21}$$

Hence the wavelength shortens as the Weber number, the product $Ca\,Re = \rho q U/\sigma$ rises, i.e. as inertia swamps capillary pressure.

3.2. *Flow on the web*

A similar analysis of flow on the web, with the same scaling and the approximate velocity profile

$$\left.\begin{aligned} u &= \frac{3}{2}\left(U_{\mathrm{R}}-\frac{1}{h}\right)\frac{y}{h}\left(\frac{y}{h}-2\right)+U_{\mathrm{R}}, \\ v &= -3h_x\frac{y^2}{h^2}\left[\left(\frac{y}{h}-1\right)\frac{1}{h}-U_{\mathrm{R}}\left(\frac{y}{3h}-\frac{1}{2}\right)\right] \end{aligned}\right\} \tag{22}$$

leads to the equation

$$h_{xxx} = 3Ca\left[\frac{\cos\beta}{\cos(\alpha+\beta)}+\left(\frac{1}{h^3}-\frac{U_{\mathrm{R}}}{h^2}\right)+\tfrac{1}{15}Re\,h_x\left(\frac{U_{\mathrm{R}}^2}{h}-\frac{6}{h^3}\right)-h_x\frac{\sin\beta}{\cos(\alpha+\beta)}\right]. \tag{23}$$

Linearizing (23) for small deviations $\epsilon \equiv \mathrm{h}-\mathrm{t} \ll t$ from the final film thickness t far downstream on the web yields

$$\epsilon_{xxx}+Ca\left[\tfrac{1}{5}Re\left(\frac{6}{t^3}-\frac{U_{\mathrm{R}}^2}{t}\right)+\frac{\sin\beta}{\cos(\alpha+\beta)}\right]\epsilon_x+3Ca\left(\frac{3}{t^4}-\frac{2U_{\mathrm{R}}}{t^3}\right)\epsilon = 0. \tag{24}$$

t of course satisfies (23) when the derivatives are all zero:

$$0 = \frac{\cos\beta}{\cos(\alpha+\beta)}+\frac{1}{t^3}-\frac{U_{\mathrm{R}}}{t^2}. \tag{25}$$

In coating operations the last two terms typically dominate, and so $U_{\mathrm{R}} \approx 1/t$. The solution of (24) then decays exponentially downstream:

$$h = t+C\exp[(A+B)\,x]. \tag{26}$$

Here
$$A,B \equiv \{-\tfrac{1}{2}b \pm [\tfrac{1}{4}b^2+\tfrac{1}{27}a^3]^{\frac{1}{2}}\}^{\frac{1}{3}}, \tag{27}$$

$$a \equiv Ca\left[\tfrac{1}{5}Re\left(\frac{6}{t^3}-\frac{U_{\mathrm{R}}^2}{t}\right)+\frac{\sin\beta}{\cos(\alpha+\beta)}\right], \quad b \equiv 3Ca\left(\frac{3}{t^4}-\frac{2U_{\mathrm{R}}}{t^3}\right), \tag{28}$$

and C can be determined if the thickness of the film at a point $x = x_0$, is known (see figure 4). When inertia and the cross-stream gravity component are neglected,

$$A \approx 0, \quad B \approx \left(\frac{3Ca}{t^4}\right)^{\frac{1}{3}}, \tag{29}$$

which is another result of Galehouse & Colt (1984).

4. Finite-element solution for the bead region

The bead region is bounded by two free surfaces, fits no standard coordinate system and cannot easily be made to do so by a global transformation. These aspects and the nature of the boundary conditions make the Galerkin/finite-element technique, suitably augmented to handle free boundaries, the method of choice for solving the system (1)–(9).

4.1. *Free-surface parametrization*

The free surfaces are parametrized by their location along conveniently placed spines (Kistler & Scriven 1983). Here the spines are taken to be straight lines, each defined by a base point $\boldsymbol{x}_{\mathrm{B}}^i$ and a direction $\boldsymbol{e}_i$, as indicated in figure 5. Along a spine the

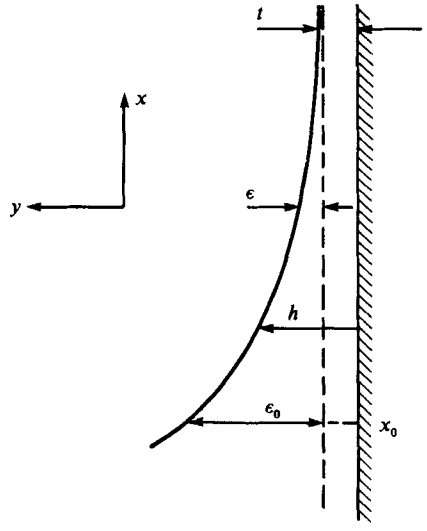

FIGURE 4. Solution of asymptotic equation far downstream on the web, $\epsilon = \epsilon_0 \exp[-|A+B|x]$.

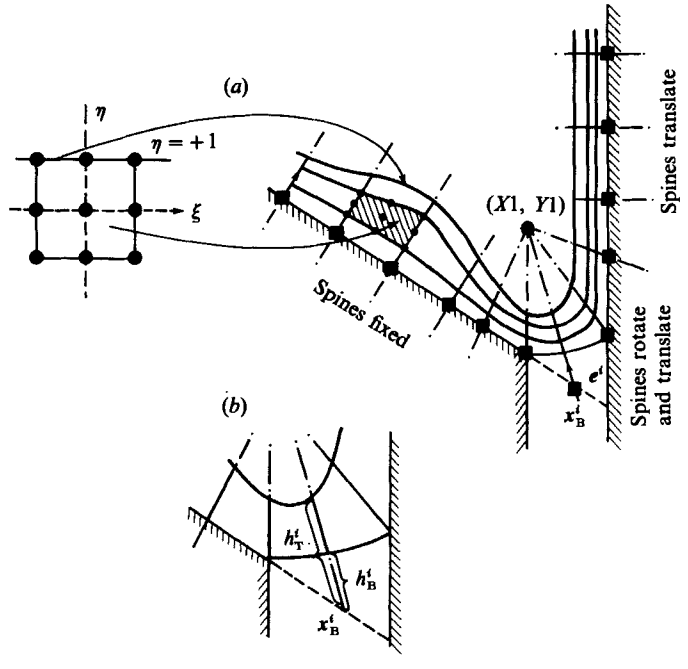

FIGURE 5. Free-spine parametrization and isoparametric mapping.

distance from the base point to a boundary is the latter's local coordinate (internal surfaces can be parametrized in the same way). In figure 5, h_T^i and h_B^i stand for the locations of the top and bottom boundaries on the ith spine. The location $\boldsymbol{x}^k$ of the node $k(i,j)$ under a free surface and on the ith spine becomes a function of the free-surface parameters:

$$\boldsymbol{x}^k = \boldsymbol{x}_B^i + [h_B^i + w^j(h_T^i - h_B^i)]\,\boldsymbol{e}_i. \tag{30}$$

w^j are the prescribed proportions according to which nodes are spaced between the base point and the free surface. In addition, the base points $\boldsymbol{x}_B^i$ and the base vectors

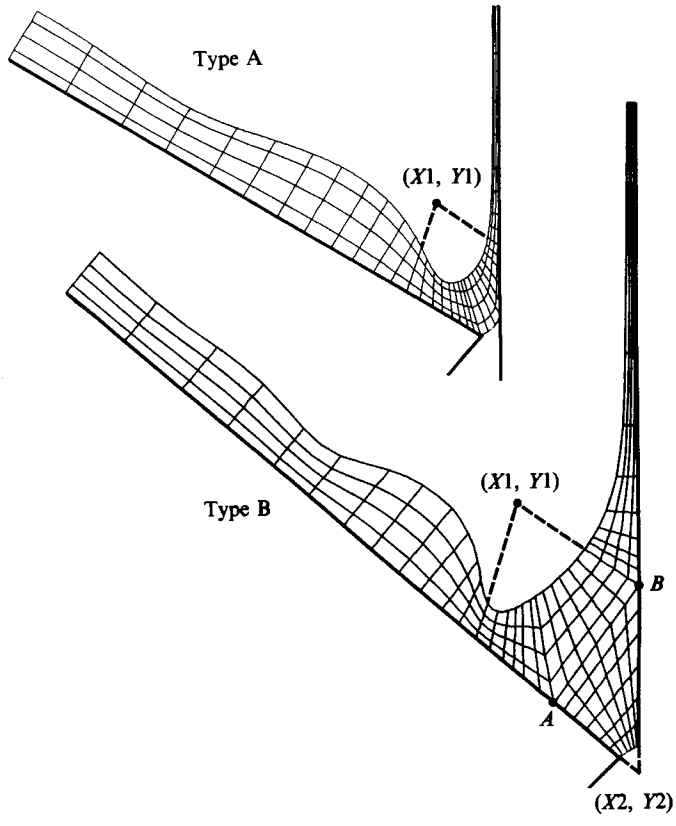

FIGURE 6. Finite-element tessellations used: type A when bead is thin, type B when bead is thick.

e_i may be functions of other parameters, such as the location x_* of the dynamic wetting line on the web. On solid boundaries, i.e. at the slide and the web, h_B^i are known. At each intersection of a spine with a free surface, however, the local coordinate becomes an unknown coefficient that must be found simultaneously with others of its kind and those that come from the basis function expansions of velocity and pressure fields described below.

A technique related to the free-spine parametrization is the method of *boundary supports* of Ruschak (1980), who in essence employed spines of fixed slopes and base-point locations. The free-spine parametrization used in this work is more flexible as it allows not only the height along each spine but also its slope and base-point location to change following the motion of free boundaries. As a consequence larger deformations of the boundaries of the flow domain can be handled before the parametrization breaks down due to excessive finite-element distortion.

Two finite-element tessellations were used here depending on the thickness of the coating bead: see figure 6. Type A tessellation was ordinarily used except at high (>50) Reynolds numbers and/or low (<4) dimensionless web speeds. At these conditions the bead is so thick as to require more resolution in the crossflow direction and then tessellation B was used.

Close to the bead in type-A tessellation it proved convenient to require spines to pass through a single point $(X1, Y1)$ so that they turn gradually from being normal

to the slide to being normal to the web. In the rest of the computational domain they were made orthogonal to the solid wall to facilitate the imposition of boundary conditions at the inflow and outflow planes. One spine was made to pass through the dynamic wetting line, wherever that was. The base point of that spine was forced to shift with the wetting line as the location x_* of the latter changed from iteration to iteration. Consequently x_* became a parameter in the base-point location and direction of each and every spine in the bead region and associated web region. This added dependence of nodal locations on the dynamic-wetting-line position had to be taken into account in order to calculate correctly the Jacobian matrix (see §4.3). Type-B tessellation had an additional region in the bead, where spines were required to pass through a second polar point $(X2, Y2)$ taken at the intersection of the extrapolation of the slide surface with the web surface. The base points in the bead were taken on a straight line AB passing through the slide edge; its slope was fixed during iteration but was manually controlled as parameters varied so that nodal points always remained inside the flow domain.

4.2. *Expansion in basis functions and isoparametric mapping*

Spines and nodes along them were so managed as to tessellate the bead region into quadrilateral subdomains, or elements, each bounded by a pair of straight sides and a pair that could be curved. Finite-element basis functions were used to approximate the solution of the Navier–Stokes system; the functions of choice were 'nine-node' biquadratic ones ϕ^i for velocity and 'four-node' bilinear ones ψ^k for pressure. This combination is a standard 'mixed interpolation' (Huyakorn *et al.* 1978):

$$\boldsymbol{u} = \sum \boldsymbol{u}_i \phi^i(\xi, \eta), \tag{31}$$

$$p = \sum p_k \psi^k(\xi, \eta). \tag{32}$$

The polynomial basis functions ϕ^i and ψ^k were constructed on a standard (ξ, η) square domain. This square was mapped into each of the deformed quadrilateral elements in the flow domain by the isoparametric mapping

$$\boldsymbol{x} = \sum \boldsymbol{x}_l(\boldsymbol{h})\, \phi^l(\xi, \eta) \tag{33}$$

where $\boldsymbol{x}_l$ are the nodal locations and $\boldsymbol{h}$ the entire set of free-surface parameters. This map allowed convenient evaluation of the free-surface location, its unit tangent vector $\boldsymbol{t}$ and normal vector $\boldsymbol{n}$:

$$\boldsymbol{t} = \frac{x_\xi \boldsymbol{i} + y_\xi \boldsymbol{j}}{(x_\xi^2 + y_\xi^2)^{\frac{1}{2}}}, \quad \boldsymbol{n} = \frac{-y_\xi \boldsymbol{i} + x_\xi \boldsymbol{j}}{(x_\xi^2 + y_\xi^2)^{\frac{1}{2}}} \tag{34}$$

as well as the derivative of any weighted residual equation with respect to the free-surface position, as is called for by the Jacobian.

The coefficients $\boldsymbol{u}_i, p_k, \boldsymbol{x}_l(\boldsymbol{h})$ were determined by requiring that the Galerkin weighted residuals vanish:

$$\boldsymbol{R}_i^{\mathrm{M}} \equiv \int_A [(Re\, \boldsymbol{u} \cdot \nabla \boldsymbol{u} - St \boldsymbol{f})\, \phi^i + \nabla \phi^i \cdot \boldsymbol{T}]\, \mathrm{d}A - \int_{\partial A} \boldsymbol{n} \cdot \boldsymbol{T} \phi^i\, \mathrm{d}s = 0, \tag{35}$$

$$R_k^{\mathrm{C}} \equiv \int_A \psi^k \nabla \cdot \boldsymbol{u}\, \mathrm{d}A = 0, \tag{36}$$

$$R_m^{\mathrm{K}} \equiv \int_{\partial A} \phi^m \boldsymbol{n} \cdot \boldsymbol{u}\, \mathrm{d}A = 0. \tag{37}$$

M, C and K stand for momentum, continuity and kinematic respectively. Essential boundary conditions were imposed by replacing the corresponding weighted residual equation with the desired velocity or free-surface specification. Natural boundary conditions were imposed through the boundary integral

$$\int_{\partial A} \boldsymbol{n}\cdot\boldsymbol{T}\phi^i \,\mathrm{d}s$$

in (35); this was obtained by applying the divergence theorem to the $\nabla\cdot\boldsymbol{T}$ term of the momentum equation (1) after it was weighted by ϕ^i and integrated over the domain A. For example, the stress boundary condition at the free surface was imposed by inserting the right-hand side of (3) into the traction boundary integral of (35). Natural end conditions on the free surface were imposed through the end terms obtained by applying the surface divergence theorem to the traction boundary condition (Ruschak 1980):

$$R_i^{\mathrm{M}} = \int_A [(Re\,\boldsymbol{u}\cdot\nabla\boldsymbol{u} - St\boldsymbol{f})\phi^i + \nabla\phi^i\cdot\boldsymbol{T}]\,\mathrm{d}A + \frac{1}{Ca}\int_{\partial A} \boldsymbol{t}\frac{\mathrm{d}\phi^i}{\mathrm{d}s}\,\mathrm{d}s - \frac{1}{Ca}(\phi^i\boldsymbol{t}_1 - \phi^i\boldsymbol{t}_0). \quad (38)$$

The end-point terms in (38) are shell forces due to surface tension. Their directions $\boldsymbol{t}_0$ and $\boldsymbol{t}_1$ had to be specified at inflow and outflow boundaries as well as at wetting lines. This procedure has worked well at static separation lines that are free to move along a solid boundary (Christodoulou & Scriven 1989*a*). But for a wide range of dynamic contact angles that might be imposed its use at the dynamic wetting line proved to prevent the iteration process from converging on a solution. And even when the process converged the dynamic contact angle of the solution often differed substantially from the angle that was to be imposed. So far the only viable alternative has been to impose the dynamic contact angle as an essential boundary condition; then, (7) becomes the extra equation required to find the dynamic-wetting-line location x_*. As viscous normal stress overwhelms capillary pressure, i.e. as capillary number $Ca = \mu U/\sigma$ becomes large, the surface region in which curvature is important shrinks to a narrowing neighbourhood of the dynamic wetting line and ultimately it becomes unreasonable to impose a dynamic contact angle at all, as Kistler found in his analysis of curtain coating. In this singular limit, the kinematic boundary condition (4) should replace (7). At the edge of the die the kinematic condition was replaced by an essential condition on the free-surface location.

Where the slip boundary condition (6) applied (ordinarily in the element adjoining the wetting line) the boundary integral

$$\int_{\partial A} \boldsymbol{n}\cdot\boldsymbol{T}\phi^i \,\mathrm{d}s$$

in (25) was split into its tangential component

$$\int_{\partial A} (\boldsymbol{t}_{\mathrm{s}}\boldsymbol{n}_{\mathrm{s}}:\boldsymbol{T})\,\boldsymbol{t}_{\mathrm{s}}\phi^i \,\mathrm{d}s$$

and the normal component

$$\int_{\partial A} (\boldsymbol{n}_{\mathrm{s}}\boldsymbol{n}_{\mathrm{s}}:\boldsymbol{T})\,\boldsymbol{n}_{\mathrm{s}}\phi^i \,\mathrm{d}s$$

at the solid surface. The tangential component was then replaced by the right-hand side of (6) and the momentum residual became

$$R_i^{\mathrm{M}} = \int_A [(Re\,\boldsymbol{u}\cdot\nabla\boldsymbol{u} - Stf)\,\phi^i + \nabla\phi^i\cdot\boldsymbol{T}]\,\mathrm{d}A + \beta_{\mathrm{slip}}^{-1}\int_{\partial A} \boldsymbol{t}_{\mathrm{s}}\cdot(\boldsymbol{u}-\boldsymbol{u}_{\mathrm{s}})\,\boldsymbol{t}_{\mathrm{s}}\,\phi^i\,\mathrm{d}s + \int_{\partial A} (\boldsymbol{n}_{\mathrm{s}}\boldsymbol{n}_{\mathrm{s}}:\boldsymbol{T})\,\boldsymbol{n}_{\mathrm{s}}\,\phi^i\,\mathrm{d}s. \quad (39)$$

The normal component (last integral in (39)) was evaluated by means of the basis-function expansion of the solution.

At the location chosen to be the inflow boundary the asymptotic film thickness and velocity profile (11*g*, *h*, *i*) could replace the kinematic and momentum residuals. Alternatively, boundary conditions of the third kind at both the inflow and outflow boundaries can be derived from the analytical solutions of the asymptotic film flow equations (17) and (26). However, this proved unnecessary at the outflow boundary: owing to downstream convection, disturbances originating downstream decay within a short distance, on the order of the film thickness, in the upstream direction (Wilson 1969). For the same reason disturbances originating upstream persist a greater distance downstream, on the order of the film thickness multiplied by the Reynolds number. Consequently only the asymptotic solution at the inflow boundary was incorporated. This was done by discarding the momentum residuals (35) at nodes on the inflow boundary in favour of the asymptotic velocity profile (13); the latter depends only on the free-surface position at the inflow plane and its derivative in the direction of the slide surface. Hence, one more equation was needed to complete the set. The kinematic condition (normally associated with that free-surface position) could not be used because it was already satisfied by (13); instead, the approximate normal stress condition (11*d*) was used. An expression for the curvature κ consistent with the assumptions that led to the linear film flow equation (14) can be found by differentiating (17) twice and eliminating ϵ_0 and ϕ among the expressions for ϵ, ϵ_x and ϵ_{xx}:

$$\epsilon_{xx} + 2\gamma\epsilon_x + (\gamma^2+\delta^2)\,\epsilon = 0, \quad (40)$$

where γ and δ are given by (18). Hence

$$\kappa \approx \epsilon_{xx} = -2\gamma\epsilon_x - (\gamma^2+\delta^2)\,\epsilon. \quad (41)$$

From (11*d*), (41) and from the definition of $\epsilon \equiv h-1$ it follows that

$$p - \frac{1}{Ca}[2\gamma h_x + (\gamma^2+\delta^2)(h-1)] = 0. \quad (42)$$

We replaced (37) with (42) at the inflow plane.

4.3. *Evaluation of the basis-function coefficients*

The integrals in (35)–(39) and (42) involve the unknown coefficients of the basis functions in (31)–(33). Area integrals were evaluated by nine-point Gaussian quadrature; line integrals, by three-point quadrature; this left a system of algebraic equations for the vector of coefficients $\boldsymbol{x} \equiv [\boldsymbol{u}, \boldsymbol{p}, \boldsymbol{h}] \equiv [u_i, p_k, h_l]$. The system was solved by Newton iteration (or a modified procedure) from an initial estimate $\boldsymbol{x}^{(0)}$:

$$\Delta\boldsymbol{x}^{(k+1)} \equiv \boldsymbol{x}^{(k+1)} - \boldsymbol{x}^{(k)} = -\omega\boldsymbol{J}^{-1}\boldsymbol{R}(\boldsymbol{x}^{(k)}), \quad (43)$$

where $\boldsymbol{R} \equiv [R_i^{\mathrm{M}}, R_k^{\mathrm{C}}, R_l^{\mathrm{K}}]$ is the vector of weighted residuals, and ω a relaxation factor that is unity in Newton iteration.

The entries of the Jacobian matrix were evaluated by Gaussian quadrature of formulas derived analytically for $J_{pq} = \partial R_p/\partial x_q$. Actually, the entries were built up as sums of contributions from the weighted residuals calculated with basis functions associated with a single subdomain, or element. These contributions constitute a submatrix known as the element-level Jacobian, which for an element adjoining the free surface has the form

$$\begin{bmatrix} \partial \boldsymbol{R}^{\mathrm{M}}/\partial \boldsymbol{u} & \partial \boldsymbol{R}^{\mathrm{M}}/\partial \boldsymbol{p} & \partial \boldsymbol{R}^{\mathrm{M}}/\partial \boldsymbol{h} \\ \partial \boldsymbol{R}^{\mathrm{C}}/\partial \boldsymbol{u} & \boldsymbol{0} & \partial \boldsymbol{R}^{\mathrm{C}}/\partial \boldsymbol{h} \\ \partial \boldsymbol{R}^{\mathrm{K}}/\partial \boldsymbol{u} & 0 & \partial \boldsymbol{R}^{\mathrm{K}}/\partial \boldsymbol{h} \end{bmatrix}.$$

For any element that does not adjoin a free surface the bottom row is absent. Evaluating the entries $\partial \boldsymbol{R}/\partial \boldsymbol{h}$ (last column) can be difficult because the weighted residuals depend on free-surface location through not only the integrands, but also the limits of integration. But if the residuals are written as integrals over the reference (ξ, η) square, correct differentiation becomes straightforward (Kistler & Scriven 1983). The correctness of the element-level Jacobian matrix was checked by numerically calculating derivatives in a few elements through a first-order differencing formula:

$$\frac{\partial R_i}{\partial x_j} = \frac{R_i(\boldsymbol{x} + \epsilon \boldsymbol{e}_j) - R_i(\boldsymbol{x})}{\epsilon}. \tag{44}$$

Here $\boldsymbol{e}_j$ is the unit vector in the jth direction and $\epsilon \ll 1$.

The linear system (43) was solved by direct factorization of $\boldsymbol{J}$ with Hood's (1976) frontal solver. The agreement of successive iterates to within a prescribed numerical tolerance (infinity norm of $\Delta \boldsymbol{x}^{(k+1)} < 10^{-6}$) was the criterion of a solution.

For Newton's method to be fully effective computationally the initial estimate $\boldsymbol{x}^{(0)}$ must fall in or near the 'ball' of quadratic convergence rate. Once a solution is at hand for one set of parameters, continuation with control of the parameter change provides a suitable initial estimate for the next set of parameters. In this work first-order or sometimes zero-order continuation was used.

First-order continuation, which usually admits larger parameter steps, starts with

$$\boldsymbol{x}^{(0)}_{\lambda+\Delta\lambda} = \boldsymbol{x}^{(f)}_{\lambda} + \frac{\partial \boldsymbol{x}}{\partial \lambda}\Delta\lambda, \tag{45}$$

where $\boldsymbol{x}^{(0)}_{\lambda+\Delta\lambda}$ is the initial approximation to the solution at the new parameter value $\lambda + \Delta\lambda$, $\boldsymbol{x}^{(f)}_{\lambda}$ is the converged solution at the previous parameter value λ, and $\partial \boldsymbol{x}/\partial \lambda$ is the solution of

$$\boldsymbol{J}\frac{\partial \boldsymbol{x}}{\partial \lambda} = -\frac{\partial \boldsymbol{R}}{\partial \lambda}. \tag{46}$$

Since in the computation the LU decomposition of $\boldsymbol{J}$ is already available from the solution at the preceding parameter value, solutions of (46) for different right-hand sides could be obtained at little extra computational cost.

What is crucial to this Newton/continuation strategy is the first solution, for which a start-up approximation $\boldsymbol{x}^{(0)}$ is needed. Ways of constructing start-up approximations are discussed by Kistler & Scriven (1983): often the construction is too rough for Newton's method to succeed. Two start-up strategies were used in this work. The first was a block Newton algorithm which is actually a variant of the Picard iteration or successive approximation, as used by Silliman & Scriven (1980). Iteration was still started as in (43) but with free-surface unknowns fixed (i.e. specified as boundary conditions). In the second iteration free-surface unknowns

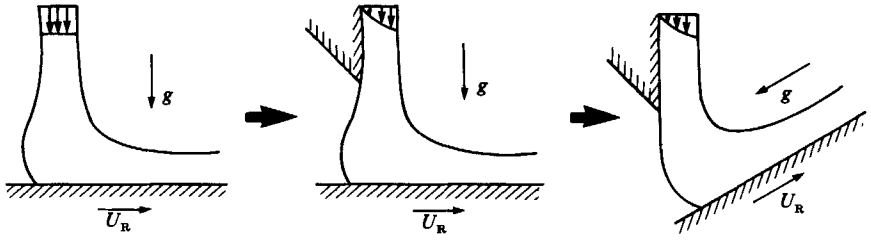

FIGURE 7. Continuation from curtain to slide coating.

were 'freed' but velocity unknowns fixed. We proceeded in this way by keeping free-surface or velocity unknowns fixed in alternate iterations until they converged. This process, which does not require the full Jacobian, converges at a much slower rate than Newton iteration but sometimes has a much larger 'ball' of convergence. In particular, when the capillary number is great enough and the kinematic formulation is used – i.e. when the kinematic condition is used to update the free-surface unknowns – this particular Picard iteration usually succeeds, as explained by Silliman & Scriven (1980).

The second start-up strategy was continuation from a related problem, a kind of 'homotopy'. A solution of a closely related equation system for the rather different configuration of a curtain coater was available from Kistler (1984). By successively converting much of the 'lower' free surface of the curtain to a slide wall, rotating the direction of gravity, and changing dimensions, the slide coater configuration was reached: see figure 7. Values of the under-relaxation factor ω in the range 0.3 to 0.5 in the first few iterations proved valuable in both strategies, for they allowed much larger incremental changes in parameters than the strict Newton/continuation strategy.

The Jacobian matrix becomes singular at bifurcation and limit points. The former can be easily detected by monitoring the determinant $\det \boldsymbol{J}$ as parameters are changed from case to case, i.e. along the solution family. This determinant changes sign at a branch point where one real eigenvalue of $\boldsymbol{J}$ becomes positive. However, we computed only two-dimensional steady flow fields, in which case bifurcation points are not generic (i.e. do not persist under perturbation of a second parameter) and hence are not easily encountered. The bead loses stability at limit points, and at Hopf bifurcation points. These are examined in forthcoming papers (Christodoulou & Scriven 1989*b*, *c*).

4.4. *Post-processing*

Streamline displays of the flow fields were constructed as contours of the stream function $\psi(x, y)$, which was computed from the velocity field by solving the linear equation

$$\nabla^2\psi = -\omega_z = \frac{\partial u}{\partial y} - \frac{\partial v}{\partial x}. \tag{47}$$

This we solved by the Galerkin/finite-element method with $\psi(x, y)$ expanded in the 'nine-node' biquadratic basis functions.

Contour plots of other kinematic and dynamic variables also facilitate the interpretation of the complex flow in the coating bead. When the finite-element representation of a variable is discontinuous at element boundaries – as are the representations of vorticity, shear stress and normal stress difference when velocity is expressed in the biquadratic basis – it can be made continuous, as we did, by the

smoothing algorithm of Chavez (1984), which produces single values f^* at nodal points from f at Gauss points by minimizing the functional

$$F = \int_A (f - f^*)\,\mathrm{d}A. \tag{48}$$

Thus f^* is the continuous and f the discontinuous approximation to the same variable. The minimization is equivalent to the easily solved linear system:

$$\int_A \sum_{j=1}^{n} \phi^i \phi^j f_j^* \,\mathrm{d}A = \int_A f\phi^i \,\mathrm{d}A, \quad i = 1, \ldots, n, \tag{49}$$

where n is the number of nodes.

To understand the dynamics of the complex flow it is valuable to see the relative importance of the forces at work – on each subdomain if not at every point (Orr & Scriven 1978). Moreover, any lack of balance of the forces is an indicator of error in the finite-element representation of the solution of the Navier–Stokes system (1)–(9). The gravitational $\boldsymbol{G}$, inertial $\boldsymbol{I}$, viscous $\boldsymbol{V}$, and pressure $\boldsymbol{P}$ contributions to the integral momentum balance on a subdomain, or element, were evaluated from ($\mathrm{d}s$ is differential arclength of the element boundary)

$$\left.\begin{aligned}
\boldsymbol{G} &\equiv \frac{1}{A_{\mathrm{el}}} \int_{-1}^{1}\int_{-1}^{1} \frac{3}{\cos(\alpha+\beta)} f J \,\mathrm{d}\xi\,\mathrm{d}\eta, \\
\boldsymbol{I} &\equiv \frac{1}{A_{\mathrm{el}}} \int_{\partial A} Re\,(-\boldsymbol{n}\cdot\boldsymbol{u}\boldsymbol{u})\,\mathrm{d}s \\
\boldsymbol{V} &\equiv \frac{1}{A_{\mathrm{el}}} \int_{\partial A} \boldsymbol{n}\cdot[\boldsymbol{\nabla u} + (\boldsymbol{\nabla u})^{\mathrm{T}}]\,\mathrm{d}s, \\
\boldsymbol{P} &\equiv \frac{1}{A_{\mathrm{el}}} \int_{\partial A} \boldsymbol{n}\cdot(-p\boldsymbol{I})\,\mathrm{d}s.
\end{aligned}\right\} \tag{50}$$

The normalization factor A_{el} is the element area, most readily obtained from the Jacobian J of the isoparametric mapping:

$$A_{\mathrm{el}} = \int_{-1}^{1}\int_{-1}^{1} J \,\mathrm{d}\xi\,\mathrm{d}\eta. \tag{51}$$

The viscous $\boldsymbol{V}^s$, pressure $\boldsymbol{P}^s$, and capillary (surface tension) $\boldsymbol{C}^s$ contributions to the surface traction balance on the free-surface side of an element were evaluated from

$$\left.\begin{aligned}
\boldsymbol{V}^s &\equiv \frac{1}{s} \int_{\partial A_{\mathrm{free}}} \boldsymbol{n}\cdot[\boldsymbol{\nabla u} + (\boldsymbol{\nabla u})^{\mathrm{T}}]\,\mathrm{d}s, \\
\boldsymbol{P}^s &\equiv \frac{1}{s} \int_{\partial A_{\mathrm{free}}} \boldsymbol{n}\cdot(-p\boldsymbol{I})\,\mathrm{d}s, \quad \boldsymbol{C}^s \equiv \frac{1}{s}\frac{1}{Ca}(\boldsymbol{t}_1 - \boldsymbol{t}_0).
\end{aligned}\right\} \tag{52}$$

Here the normalization factor s is the element-side length, which is also found most readily from the mapping (cf. (33))

$$s = \int_{-1}^{1} (x_\xi^2 + y_\xi^2)^{\frac{1}{2}} \,\mathrm{d}\xi. \tag{53}$$

5. Results and discussion

The many dimensionless parameters of design and operation that must be specified to define a case of the prototype slide coating system are listed in table 1. The results that follow illustrate the responses of the system to changes in parameters around a base case that is representative of certain practical systems: see table 2.

Two tessellations of the bead region into elements – often referred to as 'meshes' or 'grids' (of corner nodes) – generated by the free-spine method were used. They were 21×3 and 36×4, and the base-case solutions from them differed by less than 5% in any basis-function coefficient. Nevertheless the more refined tessellation was retained to resolve better the flow field at higher Reynolds numbers. It leads to 1582 equations; each Newton iteration required less than two seconds of central processor time on the CRAY-1 or later the CRAY-2 at the University of Minnesota (a midi-computer like a VAX could be used, but with less cost effectiveness). With the Newton/continuation method (§4.3), parameter changes were managed so that convergence was usually achieved in three to at most five iterations (and proceeded at a quadratic rate in the terminal stage).

Figure 8 shows the computed velocity field and streamlines for the base-case parameter set. Evidently there are standing waves at the foot of the slide whose amplitude decays in the upstream direction. On the other hand the film thickness relaxes monotonically towards its asymptotic value in the downstream direction on the web. Both features were correctly predicted by the approximate analysis of §3. The predicted velocity field and streamline contours show the deceleration of the flow under the crest of the standing wave and the acceleration under the trough. The mechanism of the rapid film thinning there can be deduced by examining contours of kinematic and dynamic variables as displayed in figures 8 and 9.

Upstream on the slide and downstream on the web the free surface is almost flat and the pressure virtually hydrostatic (figure 9*a*) in accord with the fully developed state of rectilinear flow there. The upper free surface is thus constrained by the slide surface and web inclinations. Hence the upper meniscus has to become concave in some region close to the foot of the slide and capillary pressure – the resultant of surface tension in the curved interface – gives rise to strongly subambient pressures there; this is accompanied by acceleration (figure 8*b*) and rapid film thinning. The latter provides the perturbation (ϵ_0 in (17)) from the asymptotic thickness through which capillarity gives rise to standing waves that extend upstream. The deceleration of flow under the crest of the wave and the resulting pressure increase further localizes and intensifies the pressure gradient. The normal stress difference (figure 9*b*) is small in the shear flow on the slide but becomes highly positive (extensional) near the dynamic wetting line, where contours of pressure (figure 9*a*) and shear stress (figure 9*d*) evidence the well-known singularity. Contour lines of high vorticity (figure 9*c*) signify the development of the Sakiadis-type boundary layer on the web, which was addressed by Hens & Boiy (1986). Downstream on the web the pressure excess and viscous stresses decay rapidly as the flow approaches almost solid-body translation (except for a small gravity effect).

Figures 10 and 11 show how the balancing of forces acting at free surfaces and in the bulk shifts in the different regions of the coater. Upstream on the slide all free-surface forces are small (figure 10*a*). At the crest of the standing wave capillary and pressure forces balance each other, the normal viscous stress contribution being very small. As the trough of the wave is approached normal viscous forces are turned on but still capillary and pressure forces dominate. This indicates that the standing

Parameter			Value	Base case
Final film thickness	μm	h	30–200	115.3
Web speed	m/s	U_w	0–5	1.67
Pressure difference	Pa	P_b	0–400	161.1
Clearance	mm	L	0.1–0.4	0.347
Viscosity	mPa s	μ	0.5–100	8.717
Density	g/cm^3	ρ	0.9–1.3	1.13
Surface tension	dyn/cm	σ	20–70	70.1
Dynamic contact angle	degrees	θ_d	140–160	160
Slide-web angle	degrees	α	60–80	60
Web-gravity angle	degrees	β	0–25	0

TABLE 1. Dimensional parameters and representative values for a typical slide coater system

Group	Definition	Base case
Reynolds number	$Re = q\rho/\mu$	25
Capillary number	$Ca = \mu U/\sigma$	0.0247
Pressure difference	$P_b = h_0^2 p_b/\mu q$	−90
Clearance	$L_g = L_{gap}/h_0$	0.358
Draw-down ratio	$U_R = U_w/U$	8.4
Dynamic contact angle	θ_d	160
Slip coefficient	β_{slip}	0.01
Slip length	d_{slip}	One element
Slide–web angle	α	60°
Web–gravity angle	β	0°
Units		
Length	$h_0 \equiv [3\mu q/\rho g \cos(\alpha+\beta)]^{\frac{1}{3}}$	0.969 mm
Velocity	$U \equiv [\rho g q^2 \cos(\alpha+\beta)/3\mu]^{\frac{1}{3}}$	19.905 cm/s

TABLE 2. Dimensionless parameters for the typical slide coater system

wave (or wave system) is the viscocapillary effect found by Ruschak (1978) in his analysis of film flow into a quiescent pool. However, part of the film thinning and resulting pressure gradient must stem from the liquid withdrawal by the highly extensional flow in the bead, as indicated by the increase of free-surface curvature with increasing web speed (figure 12). Downstream of the trough (figure 10*b*) viscous forces diminish but they grow again as the film levels and attains its asymptotic thickness on the web. At the same time capillary forces diminish with the curvature of the upper free surface.

Figure 11 shows how the balancing of bulk forces shifts in the different regions of the coater. The gravity force points always downwards and is drawn first; because it remains constant in the different regions of the flow it indicates the relative scaling of forces in each region. It is followed by the vectors of inertia, viscous and pressure forces as defined in (50). Upstream on the slide (figure 11*a*) the inertia force is negligible; gravity, pressure and viscous forces are of comparable magnitude but small. Under the crest of the standing wave the viscous force diminishes, as does the cross-stream velocity gradient there. Just before the locale of smallest film thickness, pressure and inertia forces are three to four times larger than the viscous and gravity forces. The pressure force, due mainly to capillarity, points downstream, i.e. from the

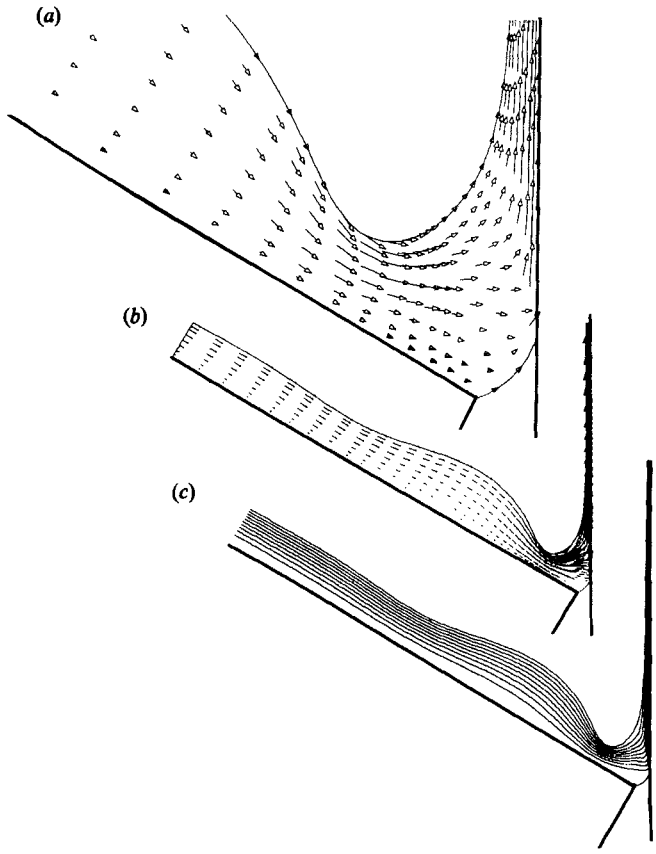

FIGURE 8. Kinematic variables of the base-case steady state: (a) velocity field, (b) velocity field in the bead region, (c) streamlines.

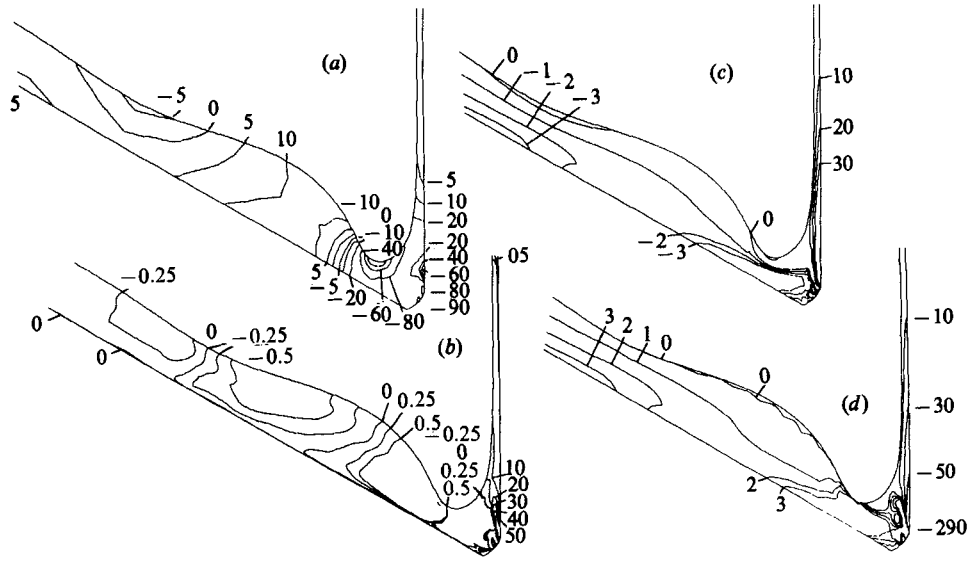

FIGURE 9. Contour lines of dynamic variables: (a) pressure, (b) normal stress difference along streamlines $\tau_{ss}-\tau_{nn}$, (c) vorticity $\partial u/\partial y-\partial v/\partial x$, (d) shear stress along streamlines τ_{sn}.

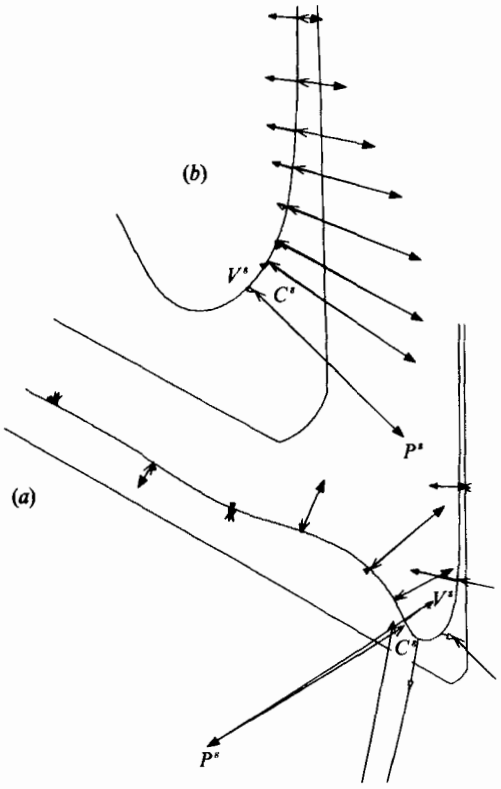

FIGURE 10. Local (element) balances of free-surface forces: (*a*) on the slide, (*b*) on the web. $\boldsymbol{V}^s$: normal viscous force; $\boldsymbol{P}^s$: pressure force; $\boldsymbol{C}^s$: capillary force.

region of the convex upper free surface to the region of the concave upper free surface. The inertia force points upstream, i.e. its direction is opposite to the acceleration it stands for. In the bead region (figure 11*b*) all forces are significant except for gravity, which is small. On the web (figure 11*c*) inertia and viscous forces dominate whereas capillarity and pressure forces diminish as the outflow plane is approached.

Surface pressure force is the difference between ambient and liquid pressure. Bulk pressure forces depend on the pressure gradients in the liquid. On the web the pressure is negative owing to the extensional flow there but nevertheless it is uniform across the film. Hence it gives rise to surface pressure forces but does not generate any appreciable bulk pressure force.

5.1. *Effect of dimensionless web speed*

The effect of varying the dimensionless web speed U_R (or equivalently the web speed at constant feed rate) is shown in figure 12. Lowering U_R lengthens the distance needed to grow a given thickness of boundary layer and thus raises the liquid inventory in the bead. Moreover, the curvature of the upper meniscus falls and the final film thickens. Obviously this process cannot be continued to zero web speeds. An approximate lower limit of operability for the web speed can be determined from (25). This can be written as

$$t^3 - \left(\frac{U_R}{c}\right)t + \frac{1}{c} = 0, \tag{54}$$

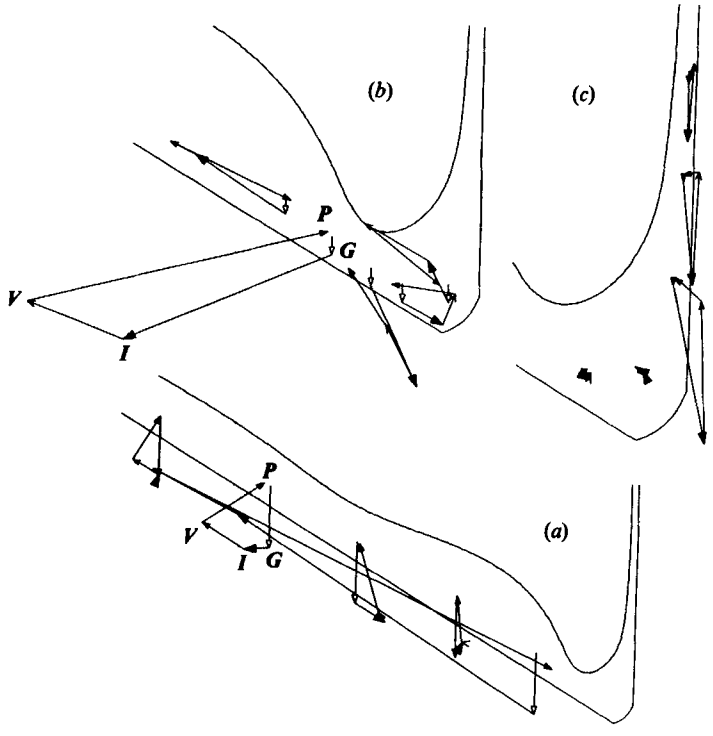

FIGURE 11. Local (element) balances of bulk forces: (*a*) on the slide, (*b*) in the bead, (*c*) on the web. ***G***: gravity force; ***I***: inertia force; ***V***: viscous force; ***P***: pressure force.

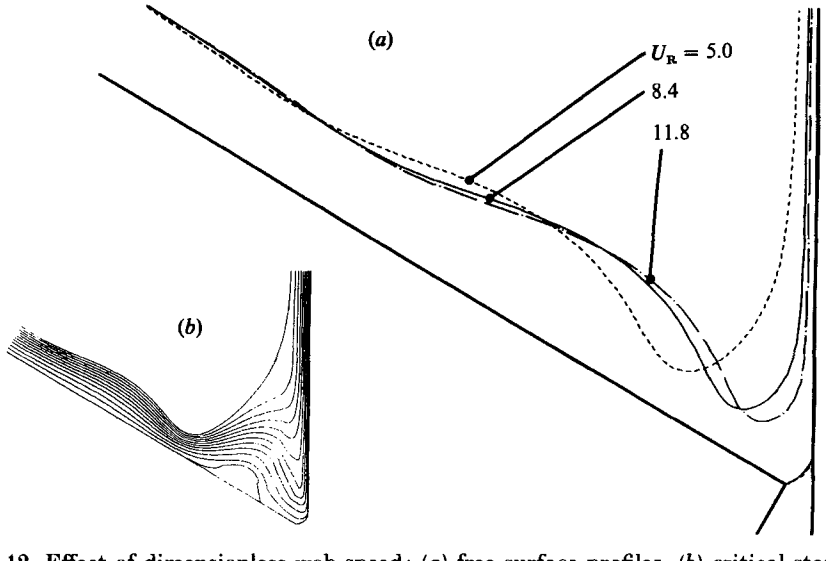

FIGURE 12. Effect of dimensionless web speed: (*a*) free-surface profiles, (*b*) critical state at low web speeds.

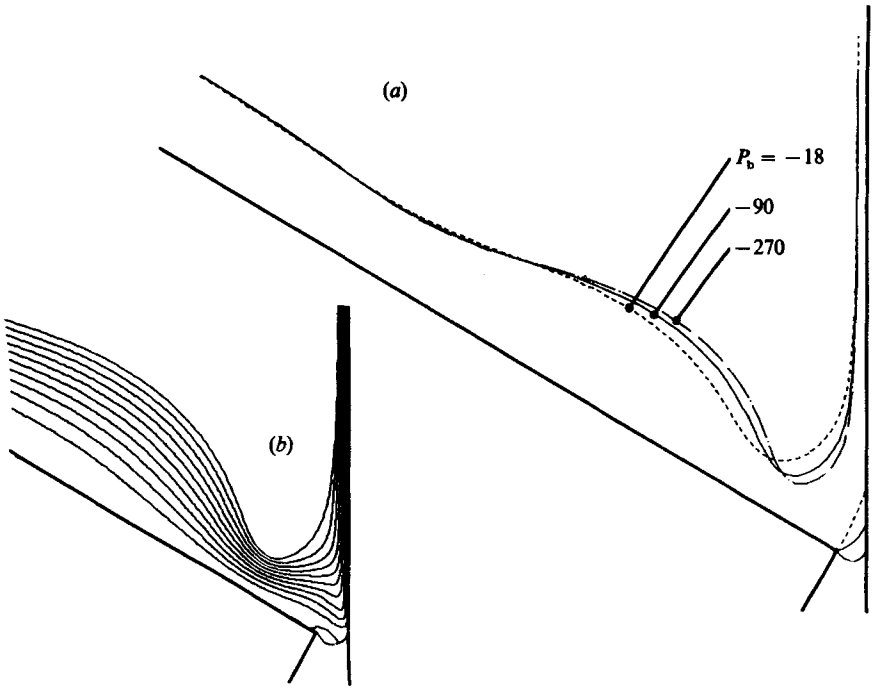

FIGURE 13. Effect of vacuum: (*a*) free-surface profiles, (*b*) heel formation at high vacuum.

c being the ratio $\cos\beta/\cos(\alpha+\beta)$. For all practical web-slide configurations – downward inclined slide and upwards inclined web – the angles α and β satisfy

$$0° < \alpha < 90°$$

and

$$-\alpha < \beta < 90° - \alpha$$

or

$$0° < \alpha + \beta < 90°,$$

so that $c \geqslant 0$. Then (54) has two positive admissible solutions when U_R is larger than $(\frac{27}{4})^{\frac{1}{3}}c$. The larger of the two predicted film thicknesses corresponds to an obstructed rising film (cf. Kistler 1980). The two roots become equal when $U_R^* = (\frac{27}{4})^{\frac{1}{3}}c$. For the base case examined here $U_R^* \approx 2.3$. This limit, however, arises in nothing more than a mass conservation principle and the assumption of a parabolic velocity profile. It is a lower bound to the actual operability limit of two-dimensional states which is shown in figure 12(*b*) and corresponds to $U_R \approx 3.7$. This was found by techniques that we shall be reporting elsewhere. Evidently recirculation regions also appear at low web speeds.

5.2. *Effect of vacuum*

By increasing the vacuum applied on the lower meniscus the curvature of both the upper and lower menisci increases as the wetting line is sucked into the vacuum chamber: see figure 13(*a*). Again the length of the boundary layer on the web increases, the liquid inventory decreases, and the thinning under the trough of the wave becomes more pronounced. Above a certain value of applied vacuum the lower meniscus forms a heel which the main liquid stream avoids by driving a small eddy near the edge of the die (figure 13*b*). The Newton iteration converged progressively more slowly and finally failed altogether as the vacuum was increased further.

When the gap is narrow – less than 0.5 mm – the results do not make clear whether

the loss of convergence at high vacuum is due to the presence of a limit point in the solution family or to inadequacy of the grid generation scheme, i.e. to the straight spines we employed in this work to parametrize effectively both free surfaces in the presence of a pronounced heel. At larger gap widths, however, the effect of gravity becomes significant and the loss of convergence is known to be due to the presence of a fold (turning point) on the solution family (Christodoulou & Scriven 1989*b*). Nevertheless, when the cut-back angle γ (see figure 2) subtended by the two solid surfaces that form the lip is not too acute, the liquid wets the lower side of the die long before the vacuum is raised to the point at which the lower meniscus becomes so curved as to make the straight spine technique inapplicable (Christodoulou & Scriven 1989*a*). This is a consequence of the Gibbs inequality condition which appears to apply also in dynamic situations (Kistler 1984).

By decreasing the vacuum almost to zero, another operability limit of steady two-dimensional states is reached. In this limit the bead loses stability to time-periodic, oscillatory states known as the 'barring' instability. Because two-dimensional, although unstable, solutions exist beyond the critical point and the determinant of the Jacobian matrix (available from the LU decomposition) does not change sign, the detection of such limits requires a separate stability analysis (Christodoulou & Scriven 1989*b*).

That the range of stable coating bead operation can be widened by imposing a pressure differential across the bead was first pointed out by Beguin (1954). He found that a small pressure differential – for instance, from 0.1 to 5 in. of water vacuum – applied to the lower meniscus appeared to prevent air entrainment, bead break-up and oscillation.

5.3. *Effect of dimensionless gap width*

The coater is usually put into operation by establishing a defect-free flow on the slide and then bringing the slide close enough to the coating roller that the liquid makes contact with the fast-moving web. Conversely the operation is stopped by increasing the distance (gap) between the slide and the roller. For a continuous operation it is essential that the gap be wide enough to allow the passage of splices without moving the slide away from the surface being coated (Beguin 1954).

Figure 14 illustrates computed predictions of the effect of changing the gap width. At narrow gaps ($L_g = 0.072 = 0.2L_0$) the static and dynamic contact-line singularities are close to each other, high negative pressures arise and the lower meniscus is almost straight. As the gap is widened, however, gravity becomes more and more important and causes the lower meniscus to bow downwards. At $L_g = 1.08 = 3L_0$ there is already a small region of slowly recirculating liquid in the lower part of the hanging bead. It grows larger as the gap width is increased further. An operability limit is eventually reached when the combined effect of vacuum, shear stress exerted by the web, and surface-tension force, cannot support the weight of the liquid bridge (Christodoulou & Scriven 1989*b*). By making the web horizontal one could widen the gap at will – while decreasing the vacuum, but then the slide coater becomes a curtain coater (Kistler & Scriven 1983), a configuration that allows large separation of the static and dynamic singularities.

5.4. *Effect of liquid inertia*

Figures 15 and 16 show the effect of varying Reynolds number. This is not equivalent to a mere change in feed rate q, which would also change the dimensionless web speed, dimensionless gap width and capillary number (table 2). The wavelength of the standing waves at the foot of the slide becomes shorter and they decay slower

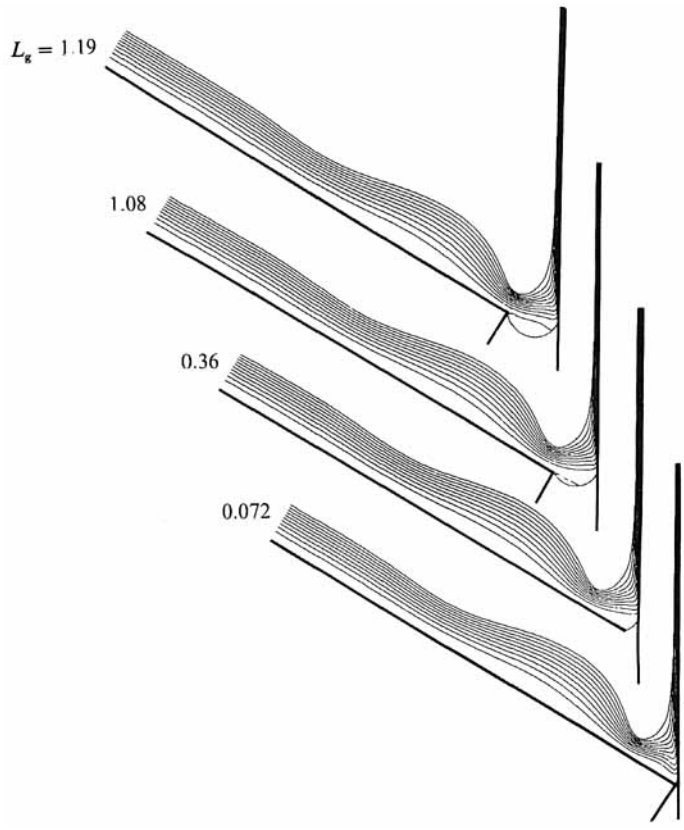

FIGURE 14. Effect of gap width on free-surface profiles and flow field.

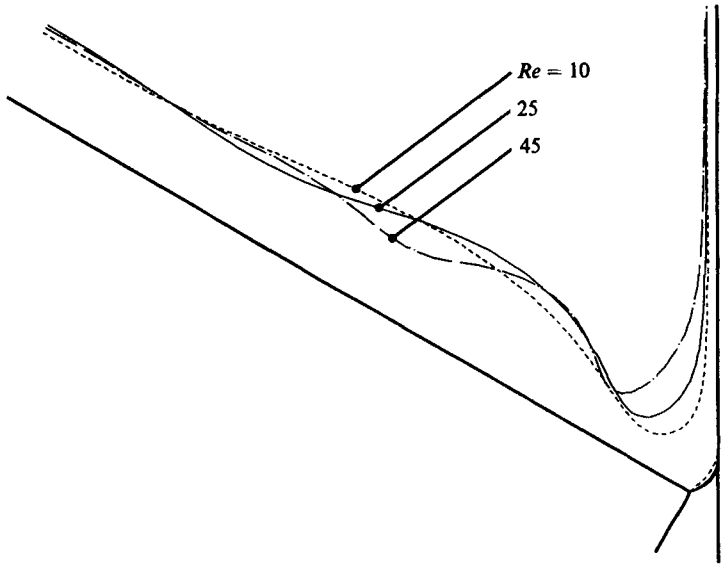

FIGURE 15. Effect of Reynolds number free-surface profiles.

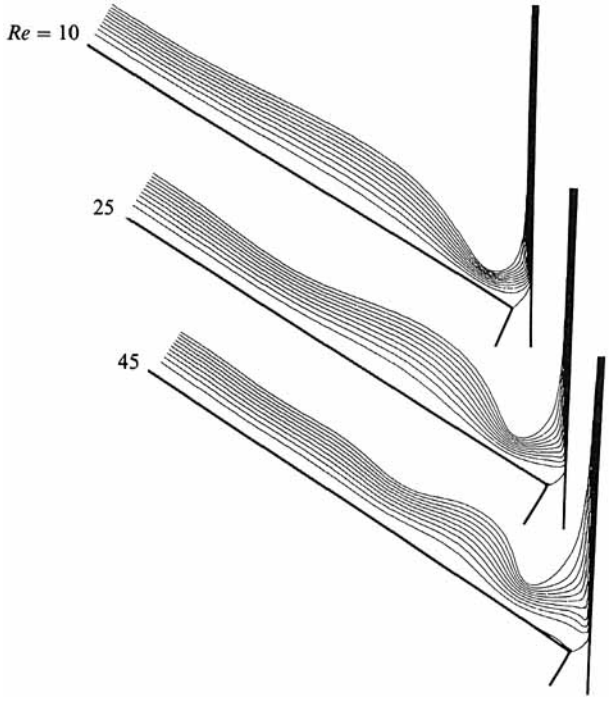

FIGURE 16. Effect of Reynolds number on flow field (streamlines).

upstream, a fact that was also predicted by the asymptotic lubrication-type analysis of §3. The film thins less just upstream of the bead because increasing liquid inertia swamps capillary pressure.

As Re is increased, convective effects dominate and the discretizations used become inadequate to resolve the various features of the flow field. This is clearly shown by local force balances (figure 17) which do not close at $Re = 35$. Further refinement was not attempted here because we judged that refinement would be inefficient without some adaptivity, i.e. tailoring to the features to be resolved.

The calculations also reveal how recirculation zones can arise on the slide, a deleterious feature that had been detected in flow visualization experiments (Schweizer 1988). These zones (eddies) grow larger as Re is raised and as slide inclination and web speed are lowered (figure 18). At those conditions there is a large inventory of liquid in the bead requiring a different mesh design in that region (figure 6).

Streamlines in figure 18 show multiple vortices, in agreement with experimental results (Schweizer 1988). One recirculation region appears on the slide under the crest of the standing wave. Because of the local thickening of the liquid film there the flow decelerates in the streamwise direction and separates at the slide wall. On the other hand at the foot of the slide a jet-like layer separates from the wall and free surface, drives two vortices there, and impinges on the web. There it splits into two streams as in flows of stagnation type (figure 18*b*). The lower stream flows downwards, opposite to the web motion, and confines close to the wall the boundary layer that would otherwise start growing right from the dynamic contact line. Ultimately it changes direction close to the contact line and feeds the boundary layer which, past the stagnation point, grows rapidly to reach the free surface.

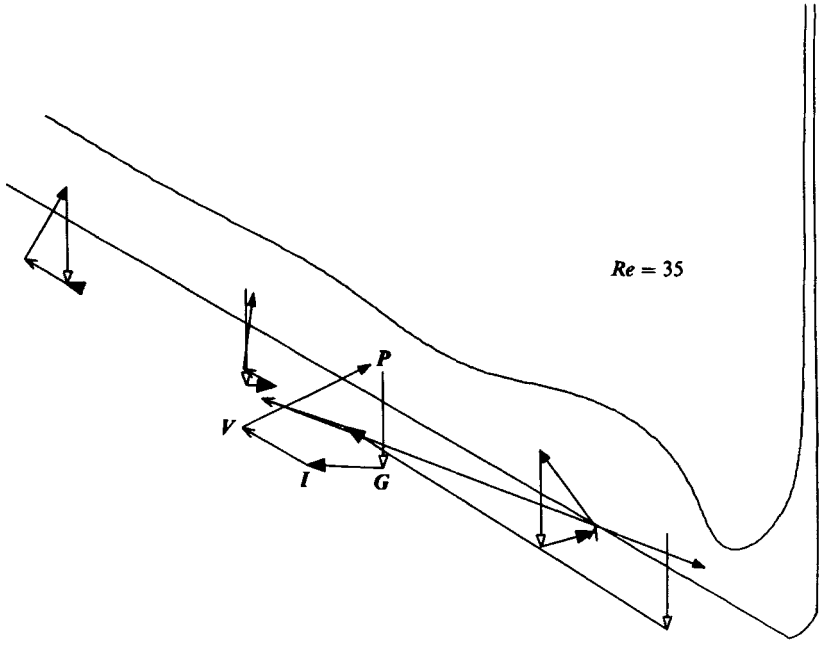

FIGURE 17. Local (element) force balances do not close at $Re = 35$.

Recirculation zones are dangerous because in them the rate of strain is relatively low and the residence time infinitely long, except for three-dimensional effects that are always present and generally cause some sort of discharge – often intermittent and local. If long residence alters the liquid the consequence can be coating defects. The core of a recirculating zone is a low-pressure region and this is another hazard, for bubbles and other low-density particles can lodge there causing flow maldistribution, especially if they coalesce or floc before being discharged. With proper design of the slide wall profile it may be possible to avoid the flow separation and formation of recirculating regions. For example, one could find the shape of slide that would maximize the minimum shear stress on the wall and the minimum particle speed along the free surface. This of course would require treating the wall surface itself as a free boundary – an almost trivial extension of the present model – whose position is governed by the optimization conditions.

5.5. *Effect of capillarity*

The fact that the standing waves are due mainly to capillarity, i.e. the resultant of surface tension in the curved meniscus, is vividly seen in figure 19. By increasing Ca – or decreasing surface tension – and keeping vacuum constant, the amplitude of the standing waves becomes smaller, their wavelength shorter, and the thinning of the film just upstream of the bead less pronounced. On the other hand, the curvature of the lower meniscus increases to compensate for the lower surface tension under the applied vacuum.

5.6. *Effect of slide and web inclination*

Slide and web inclination affect the action of gravity on the liquid layer and determine the angles at which surface tension acts at the upper meniscus. Figure 20 shows that by increasing the slide–web angle from 60° to 75° (or equivalently decreasing the slide inclination from 30° in the base case to 15°) the curvature of the

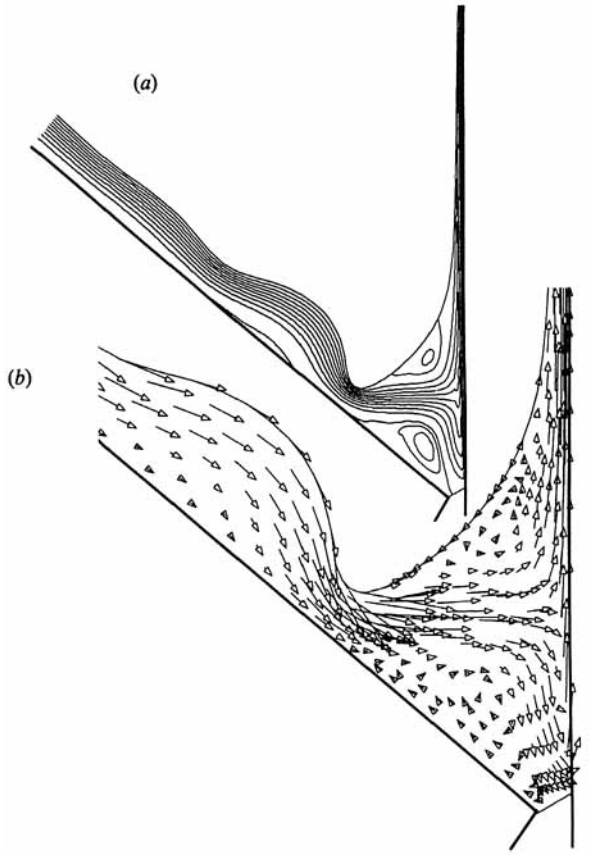

FIGURE 18. Flow field at high Reynolds number ($Re = 88$): (*a*) streamlines, (*b*) velocity field in the bead region.

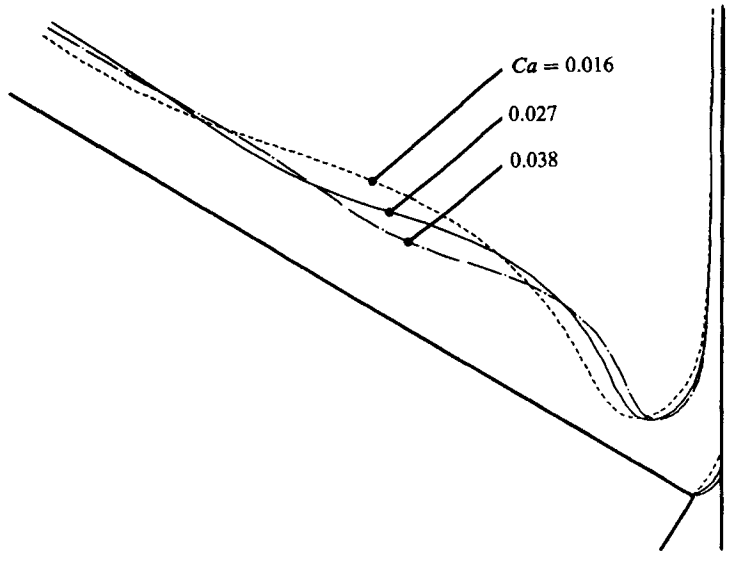

FIGURE 19. Effect of capillary number $\mu V/\sigma$ on free-surface profiles.

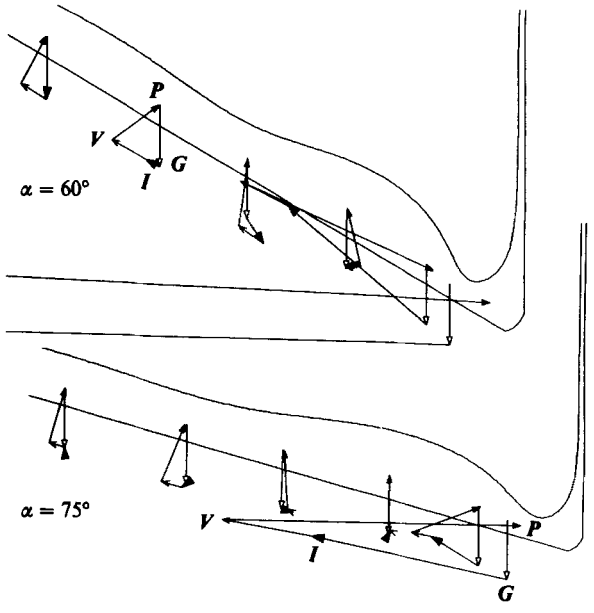

FIGURE 20. Local (element) force balances at two different slide inclinations.

upper meniscus decreases. In the same figure local momentum balances over subdomains on the slide – scaled so that gravity force remains constant – show that inertial and pressure forces fall significantly whereas viscous forces diminish scarcely at all.

The dual effect of slide inclination was pointed out by Burket *et al.* (1984). The component of the gravitational force parallel to the slide surface increases the momentum of the liquid as it impinges on the web and helps to overcome the forces that oppose deposition, namely surface tension, high shear due to the fast-moving web, and forces due to the air boundary layer along the surface of the web. The component perpendicular to the slide surface tends to even the distribution of the liquid in the transverse direction and prevents the appearance of cross-web bars. Accordingly there is an optimum inclination of the slide with respect to the direction of gravity. Matters of hydrodynamic stability of the microfluid dynamics and bifurcation of families of steady two-dimensional states to three-dimensional ones are involved, however, and these are not addressed in this work.

The effect of the empirical parameters, dynamic contact angle θ_d and slip coefficient β, are also important to examine.

5.7. *Effect of dynamic contact angle*

At finite capillary numbers it is necessary to specify an apparent dynamic contact angle – usually very different from its static value – at which surface tension acts at the dynamic wetting line. For the base-case calculation we used the value of 160°. Decreasing the dynamic contact angle, i.e. increasing the apparent dynamic wettability of the web, causes the contact length to increase (figure 21). Again, the length of the boundary layer and hence the rate of momentum transfer by viscous forces from the web to the liquid increase, causing the curvature of the upper meniscus to increase and the liquid inventory in the bead to decrease.

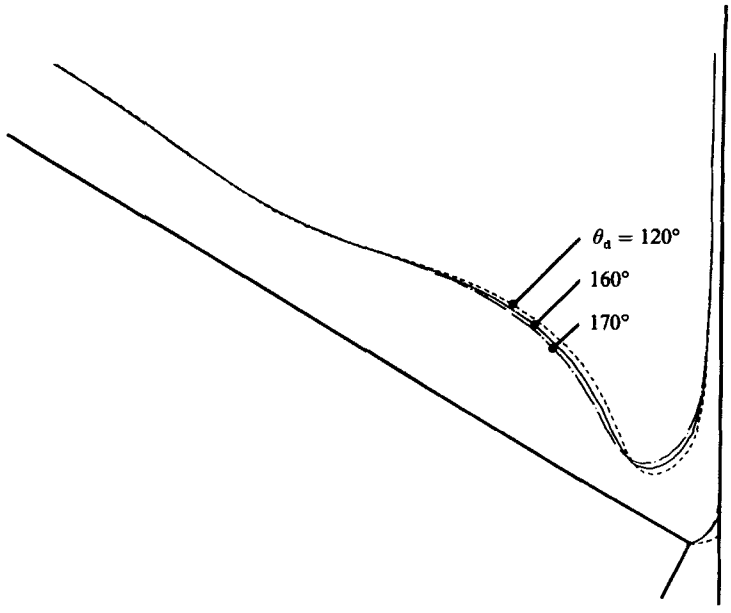

FIGURE 21. Effect of dynamic contact angle on free-surface profiles.

5.8. *Effect of slip coefficient*

In most of the analyses reported here, slip was allowed, i.e. (6) was used in place of (5) only in the first element at the wetting line. The need for a second empirical parameter is another manifestation of not accounting for the microscopic physics of the dynamic wetting process. Reducing the dimensionless slip coefficient β_{slip} by a factor of 5 or 10 from the base case value of 0.01 had no effect whatsoever on the lower meniscus and barely perceptible effect on the upper free surface (figure 22). Below the value of about 0.007, however, the liquid velocity overshot in a region around the first node downstream of the wetting line; i.e. it reached values above the web speed. Further decrease of β_{slip} to 10^{-4} and below had no effect on either the free surface or velocity distribution along the solid wall. Using such low values of β_{slip} to allow slip all along the web led to oscillations, or 'wiggles', of tangential velocity with distance downstream, the first two or three peaks exceeding the web speed. These are plainly unphysical artifacts and stem from the abruptness of the change from zero tangential velocity imposed at the wetting line to the value allowed by (6) at the first node. The lower the slip coefficient, the larger the second term in (39) and the closer the mean velocity of the liquid is forced to be to the web velocity; ultimately such a mean demands overshoot.

The difficulty is that requiring zero velocity at the wetting line gives rise to a neighbouring boundary layer that the tessellation and basis functions used cannot resolve. Tests confirmed that the lower the slip coefficient, the more refined the tessellation needed. Such refinement ought to be accompanied by refinement of the equations in order to account for the physics of the dynamic wetting process at the scale that is to be resolved; this we shall describe in a future publication. An alternative is to allow for double-valued velocity (Kistler 1984), or even multi-valued velocity at the dynamic wetting line and to use special techniques developed for representing apparent singularities as at the tips of fractures in solids (Bathe 1982).

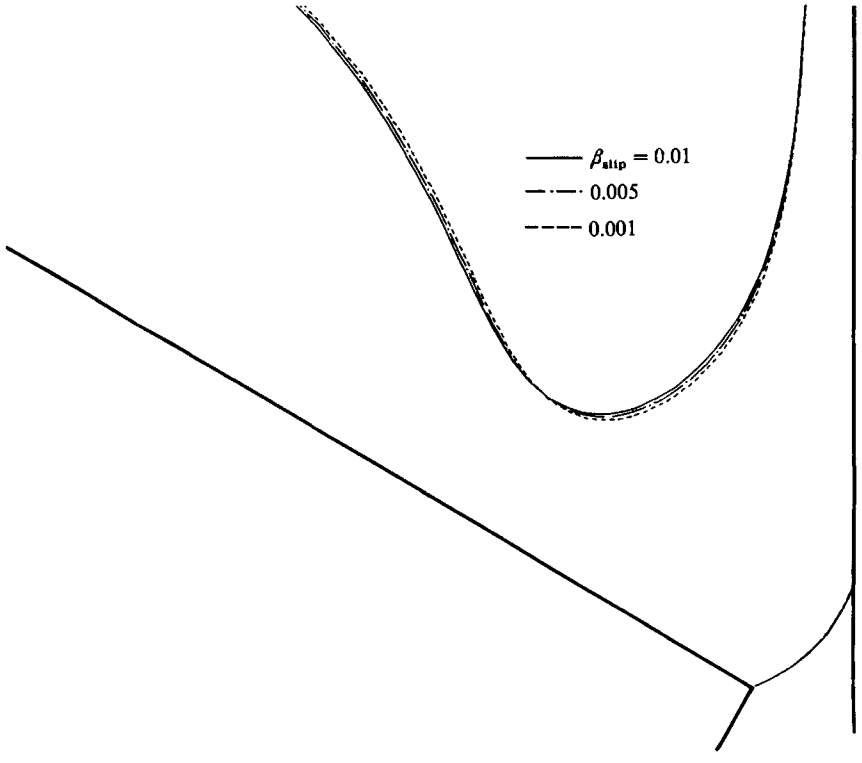

FIGURE 22. Effect of slip coefficient on free-surface profiles.

Although these expedients do not resolve the physics of the displacement process they do avoid the excessive refinement needed with a macroscopic model that relies on slip. The insensitivity of the free-surface shapes and the macroscopic flow field to the value of the slip coefficient we attribute in a future publication to the specification of a contact-angle boundary condition. There, we assume that at the limit of zero slip, Huh & Scriven's (1971) solution is valid. Although the total force exerted by the web on the liquid is predicted to be unbounded, a local momentum balance around the dynamic wetting line shows that it is a finite source of momentum. In fact the wetting line is a momentum dipole: momentum entering the liquid on the web surface is taken out on the free surface by the contact angle constraint. Because most of this transfer takes place in a small region in the vicinity of the contact line, the actual details are inconsequential to the macroscopic flow field away from that region.

6. Concluding remarks

The Galerkin/finite-element technique, spine parametrization of free surfaces, and full Newton iteration were successfully applied to describe steady, two-dimensional Newtonian flow in a slide coater. Slip and dynamic contact-angle parameters were used to relieve the non-integrable wetting-line singularity, and the lower meniscus was assumed to remain pinned at the edge of the coating die. Flow profiles show standing waves on the slide, rapid film thinning just upstream of the bead and monotonic approach to the final film thickness on the web, in agreement with

analytical solutions of the linearized film-flow equations. At high Reynolds numbers and/or low web speeds liquid accumulation in the bead increases and several recirculation regions appear, usually a deleterious effect for practical coating. Force balances over subdomains show that all four forces, namely gravity, inertia, viscous, and capillary forces, are important in the bead region, thus precluding simplification of the governing equations in most cases.

The slide coater configuration sustains variations of the flow parameters by adjusting the contact length and the inventory of liquid in the bead and ensures that liquid is picked up by the web at the same average rate as it flows on the slide; a steady state is thereby achieved. This regulatory mechanism cannot operate at any set of parameter values. Two operating limits with respect to two-dimensional disturbances were detected in this study, from loss of convergence of the Newton iteration. They were verified by eigenanalysis, i.e. linear stability theory (Christodoulou & Scriven 1989*b*). These are bead breakup at large gap widths and/or high vacuums and bead flooding at high flow rates and/or low web speeds.

Although free spine parametrization seems to work well for a wide range of parameters it becomes inadequate to parametrize highly curved meniscus shapes that accompany high back pressures. Moreover it requires the specification of a large number of mesh parameters (base points, spine angles, polar points) which themselves should be changed, ordinarily in an interactive manner, as parameters vary in order to maintain a non-singular discretization. These disadvantages can be avoided by using solution-adaptive techniques based on the solution of partial differential equations for optimizing the discretization (Thompson 1984; Christodoulou & Scriven 1989*a*).

A second common mode of operation, in which the liquid wets the underside of the lip and the lower meniscus moves freely, was not considered in this work. Wetting causes more vortices to appear in the bead but also increases the bead height and allows higher vacuums to be imposed. This could greatly reduce the danger of air entrainment. Such considerations will be elaborated in a future publication.

Full Newton iteration with its powerful by-product, the Jacobian matrix, sets the foundation for the stability analysis of slide coating flow. The ultimate goal of such an analysis is to understand – and thus to be able to control – the instabilities of thin liquid films as they are deposited and the non-uniformities of the film thickness that result: the ribbing instability that breaks the spatial symmetry of transversely uniform flow; the barring instability that is caused by oscillating coating beads and generates coatings made non-uniform by cross-web bars; and finally the air-entrainment instability that usually sets in at higher coating speeds.

We thank Willy Van Abbenyen for helpful suggestions and for a careful reading of the manuscript. The work reported here was supported by grants-in-aid from Eastman Kodak Company and Minnesota Mining and Manufacturing Company, and most recently through the Center for Interfacial Engineering of the University of Minnesota. It was also supported by the University through a Graduate Dissertation Fellowship to K. N. C. and grants for computation from the Minnesota Supercomputer Institute.

REFERENCES

Bach, P. & Hassager, O. 1985 An algorithm for the use of the Lagrangian specification in Newtonian fluid mechanics and applications to free-surface flow. *J. Fluid Mech.* **152**, 173–190.

Bathe, K.-J. 1982 *Finite Element Procedures in Engineering Analysis*. Prentice-Hall.

Beguin, A. E. 1954 Method of coating strip material. *US Patent* 2681294.

BROWN, R. A., SCRIVEN, L. E. & SILLIMAN, W. J. 1980 Computer-aided analysis of nonlinear problems in transport phenomena. In *New Approaches to Nonlinear Problems in Dynamics*, pp. 298–307. Soc. Ind. Appl. Math. Philadelphia.

BURKET, R. S., CONAGHAN, B. F. & HIRSHBURG, R. I. 1984 Coating method. *US Patent* 4443504.

BURLEY, R. & KENNEDY, B. S. 1976 An experimental study of air entrainment at a solid/liquid/gas interface. *Chem. Engng Sci.* **31**, 901–911.

CHAVEZ, P. F. 1984 On the L_2-Projection for transferring data between finite element meshes. In *Fifth Int. Symp. on Finite Element and Flow Problems, Austin, Texas, 23–26 Jan. 1984.*

CHOINSKI, E. J. 1979 Method and apparatus for coating webs. *US Patent* 4143190.

CHRISTODOULOU, K. N. & SCRIVEN, L. E. 1989*a* Discretization of viscous free surface flows and other free boundary problems. *J. Comput. Phys.* (submitted).

CHRISTODOULOU, K. N. & SCRIVEN, L. E. 1989*b* Finding leading modes of a viscous free surface flow: an asymmetric generalized eigenproblem. *J. Sci. Comput.* **3**, 355–406.

CHRISTODOULOU, K. N. & SCRIVEN, L. E. 1989*c* Operability limits of free surface flow systems by solving nonlinear eigenvalue problems. *Numer. Meth. Fluids* (in press).

FAUST, H. L. 1975 Menisci studies in bead coating. M.S. thesis, Chem. Engng Dept, Drexel University, Philadelphia.

GALEHOUSE, D. & COLT, J. 1984 Simplified analytical solutions for the free fluid surfaces associated with slide coating. *Ann. Mtg AIChE, Atlanta, Georgia, 12 March 1984.*

GUTOFF, E. B. & KENDRICK, C. E. 1982 Dynamic contact angles. *AIChE J.* **28**, 459–466.

HENS, J. & BOIY, L. 1986 Operation of the bead of a pre-metered coating device. *Chem. Engng Sci.* **41**, 1827–1831.

HENS, J. & MUES, W. 1988 Laser-Doppler measurements in the vicinity of a moving contact line. *AIChE Spring Natl Mtg, New Orleans, LA, 6–10 March, Paper* 1b.

HIGGINS, B. G. & SCRIVEN, L. E. 1979 Interfacial shape and evolution equations for liquid films and other viscocapillary flows. *Ind. Engng Chem. Fundam.* **18**, 208–215.

HITAKA, Y. & NAMIKI, T. 1984 Method for coating and an apparatus for coating. *US Patent* 4440811.

HOOD, P. 1976 Frontal solution program for unsymmetric matrices. *Intl J. Numer. Engng* **10**, 379–399 (and Correction **11** (1977), 1055).

HUH, C. & SCRIVEN, L. E. 1971 Hydrodynamic model of steady movement of a solid/liquid/fluid contact line. *J. Colloid Interface Sci.* **35**, 85–101.

HUYAKORN, P. S., TAYLOR, C., LEE, R. L. & GRESHO, P. M. 1978 A comparison of various mixed interpolation finite elements in the velocity-pressure formulation of the Navier–Stokes equations. *Computers Fluids* **6**, 25–35.

ISAYAMA, S. & TAKEHARA, N. 1981 Coating apparatus. *US Patent* 4299188.

JACKSON, B. W., WINKLER, D. E. & WOODWORTH, C. B. 1976 Apparatus of coating a multiple number of layers onto a substrate. *US Patent* 3996885.

KHESHGI, H. S. & SCRIVEN, L. E. 1979 Rising film flow – first order approximation solved. *Bull Am. Phys. Soc.* **24**, 1131.

KISTLER, S. F. 1980 Dossier in support of Ph.D. candidacy, Dept Chem. Engng & Matls Sci., Univ. of Minnesota, Minneapolis.

KISTLER, S. F. 1984 The fluid mechanics of curtain coating and related viscous free surface flows with contact lines. Ph.D. thesis, University of Minnesota, Minneapolis.

KISTLER, S. F. & SCRIVEN, L. E. 1983 Coating Flows. In *Computational Analysis of Polymer Processing* (ed. J. R. Pearson & S. M. Richardson). Applied Science Publishers.

KOBAYASHI, C., SAITO, H. & SCRIVEN, L. E. 1982 Study of Slide coating by the finite element method. *AIChE Natl Mtg, Orlando, FL, 28 Feb.–3 March, Paper* 45e.

MERCIER, J. A., TORPEY, W. A. & RUSSELL, T. A. 1956 Multiple coating apparatus. *US Patent* 2761419.

MIYAMOTO, K. 1986 On the nature of entrained air bubbles in coating. *AIChE Spring Natl Mtg. & Petro Expo '86, New Orleans, LA, 6–10 April, Paper* 86c.

MIYAMOTO, K. & SCRIVEN, L. E. 1982 Breakdown of air film entrained by liquid coated on web. *AIChE Ann. Mtg, Los Angeles, CA, 14–19 Nov., Paper* 101g.

MOFFAT, H. K. 1964 Viscous and resistive eddies near a sharp corner. *J. Fluid Mech.* **18**, 1–18.

NAVIER, C. L. M. H. 1827 Mémoire sur les lois du movement des fluides. *Mém. Acad. R. Sci. Inst. Fr.* **6**, 889.

ORR, F. M. & SCRIVEN, L. E. 1978 Rimming flow: numerical simulation of steady viscous free-surface flow with surface tension. *J. Fluid Mech.* **84**, 145–165.

PAPANASTASIOU, A. 1984 Coating flows and processing of viscoelastic liquids: fluid mechanics, rheology, and computer-aided analysis. Ph.D. thesis, University of Minnesota, Minneapolis.

RUSCHAK, K. J. 1978 Flow of a falling film into a pool. *AIChE. J.* **24**, 705–709.

RUSCHAK, K. J. 1980 A method for incorporating free boundaries with surface tension in finite element fluid flow simulators. *Intl J. Numer. Meth. Engng* **15**, 639–648.

RUSSELL, T. A., WILSON, R. M. & CARLETON, R. S. 1956 Multiple coating apparatus. *US Patent* 2761417.

SAITO, H. & SCRIVEN, L. E. 1981 Study of a coating flow by the finite element method. *J. Comput. Phys.* **42**, 53–76.

SCHWEIZER, P. M. 1988 Visualization of coating flows. *J. Fluid Mech.* **193**, 285–302.

SILLIMAN, W. J. & SCRIVEN, L. E. 1980 Separating flow near a static contact line: slip at a wall and shape of a free surface. *J. Comput. Phys.* **34**, 287–313.

THOMPSON, J. F., WARSI, Z. U. A. & MASTEN, C. W. 1985 *Numerical Grid Generation.* North-Holland.

WILSON, S. 1969 The development of Poiseuille flow. *J. Fluid Mech.* **38**, 793–806.